



---

MASTER'S THESIS

ASTROMETRIC SELECTION AND SPECTROSCOPY OF  
CANDIDATE RED QUASARS

CHRISTINA KONSTANTOPOULOU

NIELS BOHR INSTITUTE  
FACULTY OF SCIENCE  
UNIVERSITY OF COPENHAGEN

SUPERVISOR:  
JOHAN P. U. FYNBO

SUBMITTED: 11TH JUNE 2019





---

# Abstract

# CONTENTS

|          |   |           |
|----------|---|-----------|
| <b>1</b> | <b>Introduction</b>                                     | <b>3</b>  |
| 1.1      | The discovery of quasars and their properties . . . . . | 4         |
| 1.1.1    | Broad Absorption Line Quasars . . . . .                 | 5         |
| 1.1.2    | The fueling mechanism of quasars . . . . .              | 6         |
| 1.2      | Selection techniques of quasars . . . . .               | 7         |
| 1.2.1    | Optical Surveys . . . . .                               | 7         |
| 1.2.2    | Large Multicolour Surveys . . . . .                     | 8         |
| 1.2.3    | Radio and X-Ray Surveys . . . . .                       | 10        |
| 1.2.4    | Infrared Surveys . . . . .                              | 11        |
| 1.2.5    | Colour-independent Surveys . . . . .                    | 13        |
| <b>2</b> | <b>Selection, Observations and Data Reduction</b>       | <b>15</b> |
| 2.1      | Quasar Target Selection Criteria . . . . .              | 15        |
| 2.1.1    | Stripe 82 . . . . .                                     | 16        |
| 2.2      | Data Overview . . . . .                                 | 17        |
| 2.3      | Frame Processing . . . . .                              | 20        |
| 2.3.1    | Bias frames . . . . .                                   | 20        |
| 2.3.2    | Flat field correction . . . . .                         | 21        |
| 2.3.3    | Cosmic Ray correction . . . . .                         | 22        |
| 2.4      | Extraction of the spectra . . . . .                     | 24        |
| 2.4.1    | Wavelength Calibration . . . . .                        | 24        |
| 2.4.2    | Flux Calibration . . . . .                              | 27        |
| <b>3</b> | <b>Results</b>  | <b>30</b> |
| 3.1      | Spectroscopic Analysis . . . . .                        | 30        |
| 3.2      | Dust reddening . . . . .                                | 34        |
| 3.3      | The Red QSO Spectra . . . . .                           | 35        |
| 3.4      | Colour Diagrams . . . . .                               | 43        |

|                             |           |
|-----------------------------|-----------|
| 3.5 Discussion . . . . .    | 48        |
| <b>4 Conclusions</b>        | <b>51</b> |
| <b>Appendices</b>           | <b>53</b> |
| <b>A Normal Bright QSOs</b> | <b>54</b> |
| <b>B GTC Spectra</b>        | <b>57</b> |
| <b>Bibliography</b>         | <b>66</b> |



# 1 INTRODUCTION

Quasars, a subclass of Active Galactic Nuclei (AGN), are one of the brightest and most distant extragalactic objects detected to date. The study of quasars is significantly contributing to our knowledge on the star formation within their host galaxies and galaxy evolution. This makes them valuable cosmological probes and numerous surveys are dedicated to the selection and study of quasars. A common objective of these surveys has been to obtain complete and unbiased samples of the quasar population. In order to achieve that, several selection techniques have been proposed, but they all suffer from different kinds of biases. Some surveys manage to achieve high completeness of their sample, but with high contamination, while other limit the contamination, but are missing a large population of quasars.

Quasars can be reddened intrinsically or by intervening clouds (red quasars). This sub-population has been missed by multiple existing quasar surveys. The focus of this thesis is to employ astrometry combined with existing selection methods, with the aim to test this new technique of selecting red quasars.

The thesis is structured as follows: Chapter 1 includes the introduction offering an overview of the discovery of quasars and their properties. Here, the various quasar selection methods are also described. In Chapter 2, I describe the imposed selection criteria, my observations and data reduction of the candidate red quasars. In Chapter 3, I describe the results following my analysis and Chapter 4 includes the conclusions of this work. Finally, in the two appendices, I offer an overview of the additional quasar samples that were used in this thesis.

## 1.1 THE DISCOVERY OF QUASARS AND THEIR PROPERTIES

In 1963 Maarten Schmidt observed the radio source 3C 273, a stellar like object of about thirteenth magnitude and a jet with width  $1''-2''$ . The object was pointlike and so bright that it was first assumed to be a star, but further identification of the spectrum led to a redshift measurement of  $z = 0.158$  (Schmidt, 1963). The redshift indicated that the object is of extragalactic origin, and with respect to its high luminosity it was concluded that it is non-stellar. Radio and optical measurements led to the discovery of more stellar-like radio sources, like 3C 48. Greenstein and Schmidt (1964) discussed that the objects 3C 273 and 3C 48 are quasi-stellar radio sources or *quasars*.

Further studies led to the wide acceptance that quasars are among the most distant and brightest objects in the Universe. The most distant quasar to date is ULAS J1342+0928 Bañados et al. (2018), at redshift  $z = 7.54$ . Assuming the  $\Lambda$ CDM model for the accelerating expansion of the Universe<sup>1</sup>, the time elapsed since redshift  $z$  until now is

$$t(z) = \frac{1}{H_0} \int_0^z \frac{dz}{(1+z)E(z)}, \quad (1.1)$$

where  $z$  is the redshift,  $H_0$  is the Hubble constant,  $c$  is the speed of light and  $E(z)$  is the relation between the different distances defined in cosmology and can be written in terms of the  $\Lambda$ CDM density parameters as

$$E(z) = \sqrt{\Omega_r(1+z)^4 + \Omega_M(1+z)^3 + \Omega_K(1+z)^2 + \Omega_\Lambda}. \quad (1.2)$$

where  $\Omega_r$  is the radiation density,  $\Omega_M$  the matter density,  $\Omega_K$  the energy density of cosmic curvature and  $\Omega_\Lambda$  the dark energy density parameter. According to the above, the light that we detect from this distant quasar was emitted only 0.7 Gyr after the Big Bang, when the Universe was only 5% of its current age. This makes quasars an important cosmological probe, since they allow us to see far into the past of the Universe.

They are powered by the accretion disks of supermassive black holes, which lie in the center of massive galaxies. Although quasi-stellar objects (QSOs) were initially found to be strong radio sources (radio-loud), the subsequent search for stellar-like objects revealed sources that emitted too strongly in the infrared and ultraviolet relative to their brightness in the visible (radio-quiet). Quasars without strong radio emission constitute 90% of the quasar population. It is widely accepted that either radio-loud or radio-quiet, all quasars are of the same origin. They belong to the most luminous subclass of Active Galactic Nuclei (AGN), reaching a bolometric

<sup>1</sup>A  $\Lambda$ CDM cosmology is assumed throughout this thesis. The model parameters are  $\Omega_r \sim 10^{-4}$  and is negligible,  $\Omega_M=0.3$ ,  $\Omega_\Lambda = 1 - \Omega_M$ ,  $\Omega_K = 1 - \Omega_M - \Omega_\Lambda$  and  $H_0= 67.74 \text{ kms}^{-1} \text{ Mpc}^{-1}$  (Planck Collaboration et al., 2016).

luminosity of  $L_{bol} \sim 10^{47-48} \text{ erg s}^{-1}$  (or optical luminosity of  $L_v \geq 10^{11} L_{\odot}$ ). Their spectrum is characterized by strong broad emission lines, produced intrinsically by moderately dense gas. The width of the lines is a result of Doppler shifts of emitting gas particles, while their continuum is relatively flat. Quasars can be dominated by low (CII, MgII) or high ionization emission lines (CIV, SiIV). Some of the strongest observed lines in quasar spectra are  $\text{Ly}\alpha$ , CIII, CIV, SiIV and MgII. These are found in all QSO spectra, but whether they are observed or not depends on the redshift of the quasar. A typical quasar spectrum is seen in Fig. 1.1.

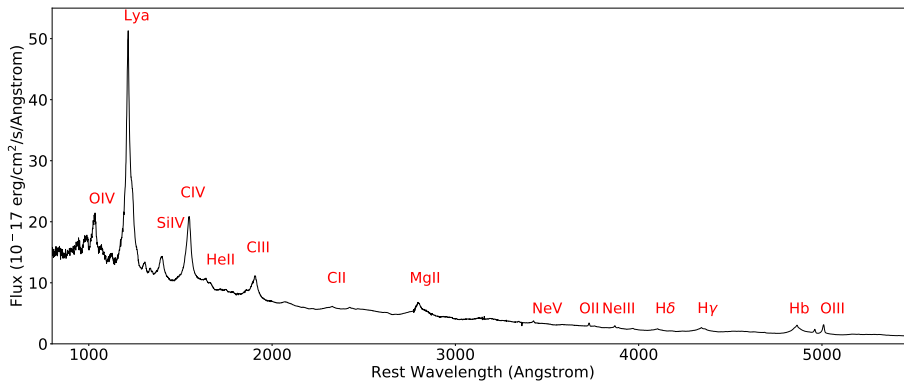


**Figure 1.1:** A composite QSO spectrum taken from (Selsing et al., 2016).

### 1.1.1 BROAD ABSORPTION LINE QUASARS

Quasar spectra may also contain absorption lines, that can be produced intrinsically or by intervening gas, which is located along the line of sight between the observer and the quasar (Weymann et al., 1981). Lines that are produced intrinsically are mainly  $\text{Ly}\alpha$  and high ionization species, like SiIV and CIV and are usually broad (BALs). However, it is seen in quasar spectra that low ionization species can also appear in BAL regions (like FeII, AlI, AlIII). Most theoretical studies suggest that these broad absorption lines come from the gas and dust accreting in a disk around the black hole (at a distance from the central source  $R \sim 0.1 \text{ pc}$  (Murray et al., 1995). Due to the high velocity of the gas near the black hole, the lines are broadened. However, recent studies show that the outflows are located to greater distances from the black hole, from several pc in the case of normal quasars to thousands pc for luminous quasars (Arav et al., 2018; Xu et al., 2018). Whether the absorption lines are produced by the quasar itself or by clouds can be distinguished by examining the spectra of the QSOs. Redshifts of the absorption

region ( $z_{abs}$ ) that are lower than the emission line redshift of the quasar ( $z_{em}$ ) indicate absorption resulting from intervening clouds, that lie in lower cosmological redshifts. This makes quasars important background sources, since possibly undetectable intervening material becomes observable through the chemical signatures of the absorption lines in the quasar spectra. The appearance of absorption lines in quasar spectra is more rare, but is very important for our understanding of the central regions of AGNs. The broad absorption regions always appear shortwards of the emission line centers, which indicates that the absorbing gas is floating outward from the nucleus (there is an outflow). The correlation of the BALs to the nuclear region could also be explained by the high ionization of the species detected in them. Around one third of the observed quasars show outflows (are BAL QSOs) (Hewett and Foltz, 2003). The broadening of the lines is a result of Doppler shifts of the gas particles, so the widths of the lines is measured in velocity units. The atoms of the gas are emitting radiation, thus they have a distribution of velocities. Depending on the velocity of the atoms relative to the observer, the observed photons may be blueshifted or redshifted. The higher the temperature of the gas, the wider the broadening of the lines. Typical narrow absorption lines have a width of  $\Delta v_{FWHM} \sim 500 km s^{-1}$ , while BALs can have widths up to  $10^4 km s^{-1}$ .

### 1.1.2 THE FUELING MECHANISM OF QUASARS

A basic characteristic of quasars is the enormous energy output, that is generated in the center of their host galaxy. At the same time it was observed that their brightness is variable on timescales as short as months, days, or even hours. This means that the total size of quasars can only be a few light-days across (Terrell, 1964). Since they are so dense and at the same time so luminous, the radiation pressure inside the quasars would be so large, that it would cause them to explode. The only way to prevent for this, is if they are very massive, at least  $10^6 M_{\odot}$ . The question of how can a solar system sized object be so massive and at the same time 100 times more luminous than a galaxy, is then explained by gravitational accretion onto supermassive black holes.

All massive galaxies have a supermassive black hole, which may be active or not, in their centers (King, 2003). Salpeter (1964) and Zel'dovich (1964) were first to propose that supermassive black holes are powering quasars. More specifically, material, like turbulent gas, is accreting around a black hole, and due to the angular momentum that is carried by the gas, an accretion disk is formed. The inner part of the disk tends to accelerate the outer part and thus angular momentum is decreasing in the inner part and increasing in the outer part. As a result, matter is flowing in the black hole and angular momentum is transferred outwards. Infalling gas will shed most of its angular momentum, through collisions, before reaching the accretion disk, where further transfer of angular momentum can occur through

viscosity. Due to viscous dissipation and friction in the disk, gravitational potential of the gas is converted to kinetic energy, compressional heating and compression of magnetic fields. This results to very high densities at small radii, and under these conditions, energy is radiated away via energetic electrons. Finally, the gas continues to spiral in, until it reaches the Schwarzschild radius and eventually falls into the black hole. One way of supplying the accretion disk with gas could also be from tidal disruption events of stars (for further reading see (Peterson, 1997)).

## 1.2 SELECTION TECHNIQUES OF QUASARS

To serve the purposes of QSO research, which are used as a probe of the Universe, large and unbiased samples need to be acquired. Many different methods have been used, since QSOs were first discovered, with the goal of building such samples. This is a challenging task, since QSOs are faint and have low surface density. This is why, the samples are built based on some selection criteria, to minimize contamination. In this section, the various selection techniques of quasars are discussed and how they are affected by different kinds of biases.

### 1.2.1 OPTICAL SURVEYS

Historically, quasars were selected based on their radio emission, since the first quasars were found to be strong radio sources. With the discovery that their optical counterparts were unusually blue, it was suggested that another way to identify quasars could be through their blue colours. Sandage (1965) found that many of the objects that he studied do not agree with the radio properties of the quasars, but are radio quiet instead. In addition, he estimated that the density of the radio quiet quasar population is actually larger than that of the radio loud. Thus, radio quiet quasars would be identified by their UV excess (UVX) relative to the stars, and not by radio properties. Although, the problems in this method were already acknowledged, since it was early realised that at large redshifts quasars would not be easily distinguished from stars, this technique has been the most common. The Bright Quasar Survey (BQS) Schmidt and Green (1983) provided the best studied quasar sample, which included 114 candidates selected based on a magnitude limit  $B < 16.16$ ,  $M_v < -23$  and on the basis of the colour criterion  $U-B < -0.44$ .

However, this method faces many problems. First, the UVX criterion is used to specifically target objects that are quasars, but not all quasars. A less strict limit would allow for a higher number of quasar selection, but also high contamination from stars. Moreover, at redshifts larger than 2.2, quasars are hard to distinguish from stars, because they appear redder. This reddening is caused by some emission lines that are redshifted in different bandpasses, and as a result contribute to the

observed flux. An example is the Ly- $\alpha$  emission, which at  $z > 2.2$  shifts to the B band and results to the increase of the U-B value. So, these quasars lose their characteristic UV excess and are missed by the UVX methods. This is clearly seen in Figure. 1.2. As a result, this method is far from complete, and different techniques are used to find quasars at higher redshifts.

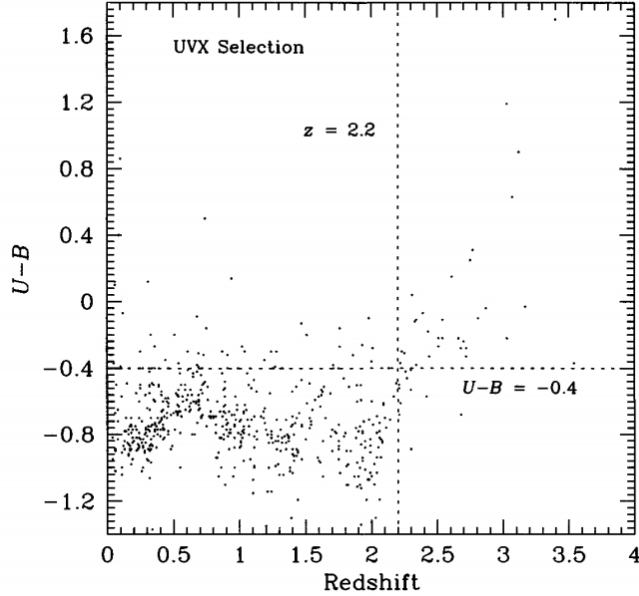


**Figure 1.2:** U-B colour as a function of redshift. The dashed lines show the UBX limit ( $U-B = -0.4$ ) and the redshift limit ( $z = 2.2$ ), above which quasars appear redder. From (Kembhavi and Narlikar, 1999).

### 1.2.2 LARGE MULTICOLOUR SURVEYS

Since the UVX method is severely incomplete, surveys that impose more than a single colour criterion are built, in order to distinguish quasars from stars.

Surveys much larger than the previous ones were built, such as the Two Degree Field (2dF) Boyle et al. (2000), and the Sloan Digital Sky Survey (SDSS) York et al. (2000), which selected their samples via the UVX technique. The goal of 2dF was to cover  $750 \text{ deg}^2$  utilizing the two colour criterion  $ubJr$ , while the SDSS goal was to cover  $10000 \text{ deg}^2$ , adopting the five band  $ugriz$  colour criterion. The purpose of these large surveys is to effectively distinguish quasars from stars, using their differences in colours.

Figure 1.3 shows the importance of u-g colour, comparing to g-r, r-i and i-z colours, in separating quasars from contaminating sources. Moreover, the u-g colour is

particularly effective for quasars at  $z < 2.5$ . It is clearly seen that at  $z > 2.5$ , quasars highly overlap with the contaminant sources and the stellar track. In fact, for the redshift range  $2.5 < z < 3$ , the purity of the quasar candidate samples drops to 10-50 % (Richards et al., 2006). Moreover, the two surveys, since they based their selection on the UVX criterion, are biased against dust reddened quasars and they are not included in the samples.

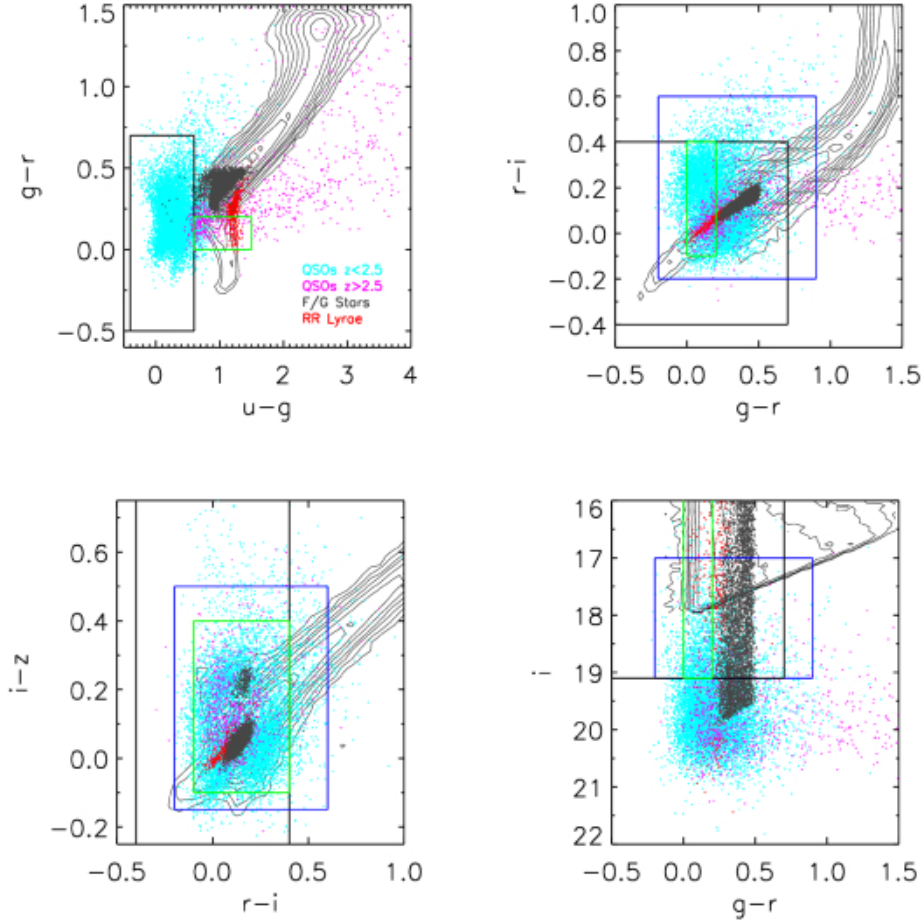


**Figure 1.3:** Point sources from the SDSS Stripe82 in the ugriz colour space. The  $z < 2.5$  spectroscopically confirmed quasars are illustrated in light blue, while quasars with  $z > 2.5$  are shown in magenda. The contaminant point sources are shown in grey, and the stellar track with black contours. From (Schmidt et al., 2010).

In addition, the use of Automatic Plate Measuring (APM) machines led to the significant increase of the speed that quasar spectra are collected. Due to these,

large and more complete samples of quasars became available, which allowed for the development of large surveys. Moreover, the combination with multicolour criteria led to the discovery of higher redshift quasars. The first quasar with redshift  $z=4$  was discovered using multicolour data derived from measurements of photographic plates taken from the United Kingdom Schmidt Telescope (UKST) (Warren et al., 1987).

### 1.2.3 RADIO AND X-RAY SURVEYS

Identifying quasars through their radio and X-Ray emission has also developed, since their emission in these wavelengths is much stronger than in stars and galaxies. The procedure in these surveys starts with the development of a catalog of sources, with accurately determined positions of  $\sim 1''$  on the sky. Then, these sources are cross-matched with existing optical catalogs, where the candidates are spectroscopically examined until the identification of the quasar is confirmed and its redshift is then determined.

The advantage of this method is that it is not biased against dust reddened or high redshift quasars, like the optical surveys. As discussed above, quasars were first discovered as strong radio sources, but was soon realized that the radio-loud quasars constitute only  $\sim 10\%$  of the overall population. This makes radio surveys highly incomplete, since radio-quiet quasars are not detected with this method. However, with the development of deep wide field surveys, like FIRST (Becker et al. (1995)), this method gained more ground. The flux sensitivity of FIRST reaches to milli-Jansky limits, and with this sensitivity even radio-quiet quasars can be detected. Radio (FIRST) and optical data (SDSS) were combined in Ivezić et al. (2002), which revealed that most of the optically unresolved radio sources have non-stellar colours, which indicates that they are quasars. In addition, optical colour differences between radio-loud and radio-quiet quasars in the same redshift range were found. However, as the optical brightness decreases, the fraction of the quasars that are identified drops to just  $\sim 10\%$ , which makes this method highly incomplete.

X-ray surveys also gained importance, since it was discovered that X-ray emission is originated in the vicinity of the central black hole. The first results for the search of bright quasars, that are identified by their X-ray emission measured in the ROSAT All-Sky Survey, are presented in (Grazian et al., 2000). Following ROSAT, Chandra (Weisskopf et al. (2002)) and XMM-Newton (Jansen et al. (2001)) satellites, detected sources that were previously missed by optical surveys. These deep X-ray surveys achieved a combination of much higher sensitivity (50-250 times higher) than the previous X-ray surveys, position accuracy and large samples. Deep X-ray surveys can detect quasars that are less luminous than the ones

detected in optical surveys, and combined with wide field surveys, this leads to the detection of quasars in a wide range of luminosities. The XMM-Newton COSMOS Survey [Hasinger et al. \(2007\)](#) and the Chandra COSMOS Survey (C-COSMOS) [Elvis \(2009\)](#) use a combination of high resolution X-ray imaging and the COSMOS photometric and spectroscopic database, which covers a  $2 \text{ deg}^2$  equatorial field, to detect very faint quasars. Finally, the Chandra COSMOS Legacy Survey [Civano et al. \(2016\)](#) covers an area three times larger than previous surveys at similar depth, and its depth is three times fainter than surveys covering similar area. X-ray surveys remain an efficient way of detecting quasars, and they only show bias against highly obscured Compton-thick AGN.

#### 1.2.4 INFRARED SURVEYS

As explained above, quasar selection based on their UV-excess has been quite unsuccessful in detecting dust-obscured quasars. Longer wavelengths are less affected by dust extinction and, as a result, selecting quasar candidates using near-infrared (NIR) criteria became important with the development of datasets of sufficient depth and coverage.

The Two Micron All-Sky Survey (2MASS) [Skrutskie et al. \(2006\)](#) uniformly scanned the whole sky in the J ( $1.25 \mu\text{m}$ ), H ( $1.65 \mu\text{m}$ ) and Ks ( $2.16 \mu\text{m}$ ) near-infrared bands, to detect and characterize point sources brighter than  $\sim 1 \text{ mJy}$  in each band. This means that 2MASS will only detect the brightest quasars.

The United Kingdom Infrared Telescope (UKIRT) Infrared Deep Sky Survey (UKIDSS) [Lawrence et al. \(2007\)](#) is a successor to 2MASS, and has a 3 times fainter magnitude limit than 2MASS in the K-band. One of the UKIDSS objectives was to detect the highest redshift quasars and it provides the ground for creating a large NIR selected quasar sample.

In analogy to the UVX method at shorter wavelengths, quasars are also selected based on their K-band excess (KX) compared to stars ([Warren et al., 2000](#)). In the KX method [Maddox et al. \(2008\)](#), the fact that quasars appear much redder than stars in J-K is exploited, since quasars and stars are clearly separated in the colour diagrams, plus the separation is increasing with dust reddening. This method effectively selects red quasars, distinguishing them from stars. However, the effectiveness drops, when trying to distinguish quasars from galaxies, since the colour distribution of the faint galaxies often overlaps that of quasars, as seen in [Figure 1.4](#). This problem is resolved by utilizing morphological information, since low-redshift galaxies are resolved. Another problem is the brightness of the host galaxy, which is larger in the K-band than the optical and in this case faint quasars are not detected and underrepresented in the sample. Nevertheless, the reduced extinction in the K-band, makes the KX method capable of including a much larger fraction of red quasars than optical surveys.

The Wide-field Infrared Survey Explorer (WISE), a satellite launched by NASA in 2009, completed a mid-infrared survey in four bands (W1,W2,W3,W4) covering the entire sky, achieving much higher sensitivity than any previous infrared mission (Wright et al., 2010). AGNs have been selected based on a MIR colour criterion  $W1-W2 \geq 0.8$  (Vega), identifying 78 % of the AGN candidates with 95 % reliability (Stern et al., 2012). The other method was developed by (Mateos et al., 2012), who used two MIR colour criteria (W1-W2 and W2-W3). MIR selection is effectively separating quasars from stars and galaxies, is less affected by dust extinction and is more effective in finding high redshift quasars. However, like all selection methods, MIR selection also suffers from biases, and can not produce a sample that is both complete and reliable. It has been shown that many X-ray sources have similar MIR colours with galaxies (particularly star-forming galaxies), and as a result are missed by MIR selection criteria (Barnby et al., 2006). Lacy et al. (2004) also used mid-infrared criteria, aiming for high completeness, but with the cost of low reliability.

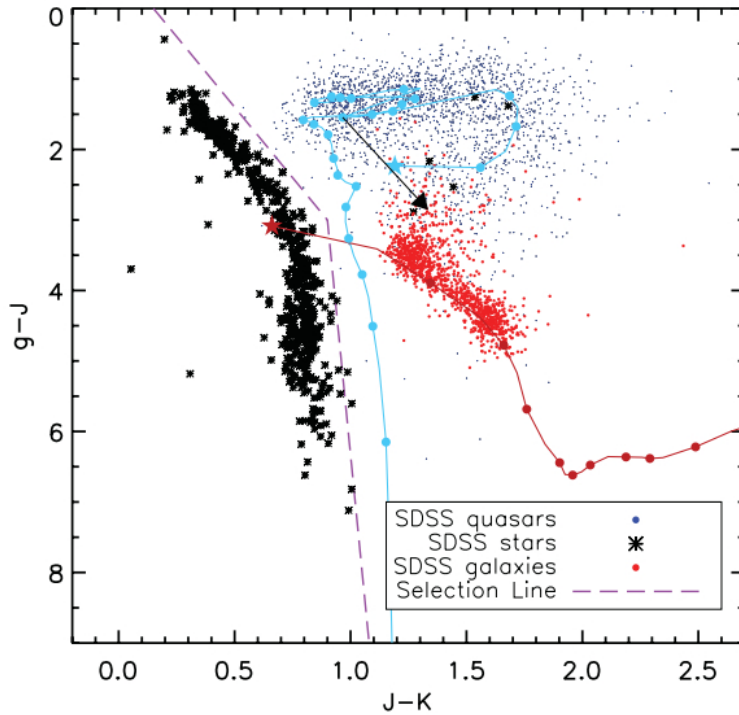


**Figure 1.4:** The KX based selection of candidate quasars. The plot shows the clear separation of quasars from stars, and the overlap of quasars and low-redshift galaxies. The black arrow indicates that the dust reddening increases the separation. From (Maddox et al., 2012).

### 1.2.5 COLOUR-INDEPENDENT SURVEYS

Smith (1975) and Osmer and Smith (1976) developed the Objective Prism Survey, which focused on the detection of strong emission lines in the quasar spectra, as a colour-independent method of selecting them. In this method quasars are selected by identifying emission lines, most commonly Ly- $\alpha$ , and the redshift range of the identified quasars is  $1.8 < z < 3.3$ . The slitless spectroscopic technique, although is quite efficient in finding high redshift quasars, it suffers from a selection bias against quasars with weak or no emission lines, so these objects are missed from the survey. Also, the signal-to-noise ratio of slitless spectra is limited.

Quasars are also found to vary in brightness on timescales of months or years, so another selection method that has been explored is their variability. This property alone can be used to identify quasars, and has proven to be very effective, in terms of both completeness and purity. Many physical mechanisms have been proposed to explain variability of quasars, including accretion disk instabilities Rees (1984), starbursts in the host galaxy Aretxaga (1997) and gravitational microlensing from intervening bodies (Hawkins, 1996). Although variability alone appears to be 90% complete and 95% pure for quasars that show UV-excess Schmidt et al. (2010), it has also been combined with other detection methods like radio and objective prism surveys, to obtain variability independent samples. The advantage of this method is that it does not depend on the colours of the quasar candidates and as a result can be used over a broad range of redshifts, including the redshift range  $2.5 < z < 3$ , the 'quasar desert' in colour selected samples. Identifying quasars using variability is 90% complete and 96% pure in this redshift range (Schmidt et al., 2010).

The most recent colour independent method of selecting quasars is using their characteristic zero proper motion. Since quasars are very distant objects, their proper motion is negligible, and they appear to be stationary. On the contrary, Galactic stars show a significant amount of proper motion in the sky. As a result, the proper motion criterion is very important for eliminating stellar contamination from the quasar samples, which has been a major objective of many previous studies. Using proper motion as a selection criterion has already been proposed by Kron and Chiu (1981), who surveyed  $0.1 \text{ deg}^2$  of the sky for faint quasars. Although they used this method, they found quasars that could have been detected by other existing methods instead, while their sample suffers from significant stellar contamination. Thus, their survey is only  $\sim 20\%$  effective. The problem that this method was facing is the lack of measured proper motion, as well as the large error in the proper motion measurements, which leads to low accuracy data.

This changes with the launch of ESA's Gaia satellite in 2013, whose mission is to make a three dimensional map of the Milky Way and provide with unprecedented measurements of position and proper motion of about 1 billion stars in our Galaxy

and the Local Group (Gilmore et al., 2012). Star's positions and motions are measured 200 times more accurately than the preceding Hipparcos mission (Perryman et al., 1997), that was launched by ESA in 1989. As calculated by Heintz et al. (2015), for  $G=20$  mag, the lower limit of proper motion error is  $\sim 0.3$  mas/yr, while for  $G=18$  mag, it is  $\sim 0.1$  mas/yr. Gaia is limiting the error of proper motions significantly, which increases the efficiency of the quasar selection based on proper motion. This method allows for the development of a completely unbiased quasar sample in terms of colour, and as a result is very important for the selection of red quasars, eliminating stellar contamination. The efficiency of this selection technique for the selection of red quasars will be characterized in the following chapters.

# 2 SELECTION, OBSERVATIONS AND DATA REDUCTION

## 2.1 QUASAR TARGET SELECTION CRITERIA

The candidate quasars were selected for observation, based on specific criteria, including colour and astrometry. The aim was to target reddened quasars, as well as, reduce the stellar contamination. Photometry was used from the optical SDSS DR12 (Eisenstein et al., 2011), the near-infrared (NIR) UKIDSS DR1 (Warren et al., 2007) and the mid-infrared (MIR) WISE data release (Wright et al., 2010). The SDSS optical bands are  $u, g, r, i, z$ , with effective wavelengths 3543 Å, 4770 Å, 6231 Å, 7625 Å and 9134 Å respectively. The UKIDSS NIR bands are  $Y, J, H, K$ , with effective wavelengths 1.02  $\mu m$ , 1.25  $\mu m$ , 1.63  $\mu m$  and 2.2  $\mu m$ . The WISE MIR bands are  $W1, W2, W3, W4$ , with effective wavelengths 3.4, 4.6, 12 and 22  $\mu m$  respectively.

First, the optical colour criteria  $u-g > 1$ ,  $r-z > 0.5$  are imposed to specifically target dust-reddened quasars, as they are expected in optical colour space, while the  $r < 20$  cut is chosen for targets that are bright enough for observation. The optical criterion  $g-r > 1$  is imposed to target a region poorly studied for red quasars. Then, the MIR cut  $W1-W2 > 0.8$  is applied to effectively separate quasars from stars in MIR colour space, and reject low redshift QSOs.

Additionally, the astrometric data from Gaia are used, and specifically the characteristic zero proper motion of quasars as opposed to stars, to further reduce stellar contamination. To apply this, objects whose proper motion deviate from the mean proper motion error by more than  $3\sigma$  are rejected. The selection criteria are summarized in Table 2.1.

| Criterion            | Application              |
|----------------------|--------------------------|
| $r < 20$             | Bright limit             |
| $u-g > 1, r-z > 0.5$ | Target Red QSOs          |
| $g-r > 1$            | Target Red QSOs          |
| $W1 - W2 > 0.8$      | Separate QSOs from stars |
| $pm/epm < 3$         | Separate QSOs from stars |

**Table 2.1:** The optical, MIR and astrometric selection criteria.

### 2.1.1 STRIPE 82

The chosen area for the search of red quasars is Stripe 82, an area that covers  $300 \text{ deg}^2$  on the Celestial Equator in the Southern Galactic Cap ( $-50 \text{ deg} < \text{R.A.} < 60 \text{ deg}$ ,  $-1.25 \text{ deg} < \text{Dec} < 1.25 \text{ deg}$ ). The fields at  $\text{R.A.} > 300 \text{ deg}$  are excluded, because they are close to the Galactic plane, so they contain Galactic stars and dust. The chosen area has been scanned by SDSS repeatedly ( $\sim 70\text{-}90$  times) in the five (ugriz) bands, searching for quasars, and it is considered that most of the quasars in this area have already been found. So, this field is chosen to further test the above selection criteria, on their effectiveness in finding red quasars, in a field excessively investigated over the years. The location of the SDSS spectroscopically confirmed QSOs along with the NOT targets are shown in ICRS Celestial coordinates in Figure 2.1.

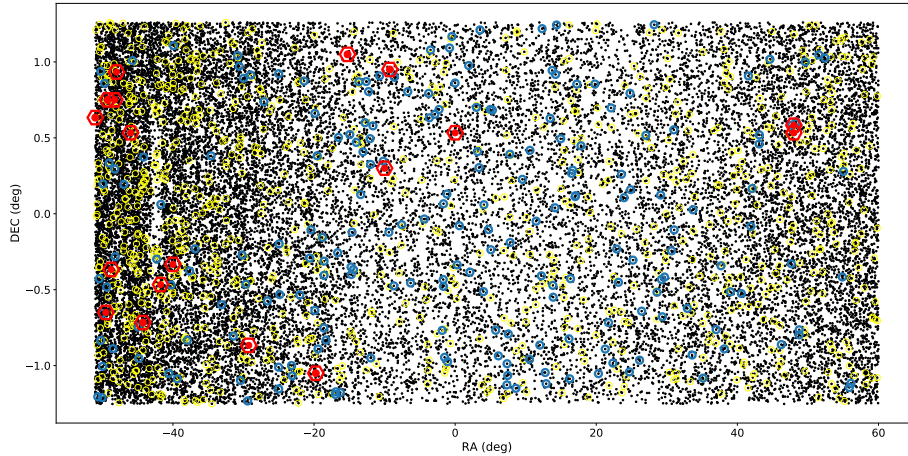


**Figure 2.1:** The field of Stripe82 in Celestial coordinates. The black dots are all the sources in the field within  $3\sigma$  of proper motion and  $g > 16$ . The yellow circles show the stars, the blue circles are the SDSS spectroscopically confirmed QSOs and the red hexagones are all the targets observed at the NOT.

## 2.2 DATA OVERVIEW

The data were obtained with the 2.5m Nordic Optical Telescope (NOT), operated by the Spanish Observatorio del Roque de los Muchachos in La Palma. They were observed during the Danish Summer School in Observational Astronomy over the period of the 14th to 17th of August 2018. The telescope was equipped with the Andalucia Faint Object Spectrograph and Camera (ALFOSC) for low/medium resolution spectroscopy. Grism #4 was used, that covers the wavelength range from 3200 Å to 9600 Å, while the slit was mostly 1.0", giving a resolution of  $R = \frac{\lambda}{\Delta\lambda} = 360$ . A slit of 1.3" was also used when the seeing conditions required it, i.e significantly above 1". The targets were selected based on specific selection criteria that are discussed in 2.1. Finding charts are used to identify the objects' position in the sky, after the guiding star has been targeted. An example of a finding chart is seen in Figure 2.2. The aim for the signal-to-noise ratio (SNR) was at least 10 for magnitudes around 600nm, so the exposure times were calculated accordingly. Two exposures of each target were obtained, to allow robust detection of emission lines. In total, 12 candidate red quasars were observed, and 6 candidate normal bright quasars are used for completeness of the sample and comparison purposes. The corresponding standard star data were also obtained each night, as well as the bias, flat field and arc frames required for calibration. The complete

list of the quasar data observed is shown in Table 2.2.

| Target           | Exposure time [s] | $r_{SDSS}$ (mag) | Grism | Slit | Airmass |
|------------------|-------------------|------------------|-------|------|---------|
| RedJ0000+0032    | 2x600             | 19.34            | 4     | 1.0" | 1.22    |
| RedJ2047+0045    | 2x400             | 18.40            | 4     | 1.0" | 1.52    |
| RedJ0312+0035    | 2x900             | 19.81            | 4     | 1.3" | 1.38    |
| RedJ0312+0032    | 2x800             | 19.39            | 4     | 1.0" | 1.26    |
| RedJ2045-0022    | 2x200             | 18.30            | 4     | 1.0" | 1.47    |
| RedJ2056+0032    | 2x600             | 19.55            | 4     | 1.0" | 1.31    |
| RedJ2113-0028    | 2x900             | 19.79            | 4     | 1.0" | 1.20    |
| RedJ2120-0020    | 2x400             | 18.25            | 4     | 1.0" | 1.47    |
| RedJ2320+0018    | 2x900             | 19.77            | 4     | 1.3" | 1.16    |
| RedJ2042-0039    | 2x700             | 19.31            | 4     | 1.0" | 1.15    |
| RedJ2203-0052    | 2x600             | 18.69            | 4     | 1.0" | 1.35    |
| RedJ2048+0056    | 2x700             | 19.32            | 4     | 1.0" | 1.14    |
| BrightJ2036+0038 | 2x200             | 18.95            | 4     | 1.0" | 2.35    |
| BrightJ2323+0057 | 2x200             | 18.95            | 4     | 1.0" | 1.16    |
| BrightJ2103-0043 | 2x200             | 17.28            | 4     | 1.0" | 2.21    |
| BrightJ2241-0103 | 2x200             | 18.32            | 4     | 1.0" | 1.45    |
| BrightJ2259+0103 | 2x200             | 18.64            | 4     | 1.0" | 1.43    |
| BrightJ2043+0045 | 2x200             | 18.77            | 4     | 1.3" | 1.18    |

**Table 2.2:** The observed targets. Presented are the name of the target, the magnitude in the r band, the grism and slit that was used and the airmass during each target observation.

| Target           | RA       | DEC       |
|------------------|----------|-----------|
| RedJ0000+0032    | 00:00:00 | +00:32:00 |
| RedJ2047+0045    | 20:47:00 | +00:45:00 |
| RedJ0312+0035    | 03:12:00 | +00:35:00 |
| RedJ0312+0032    | 03:12:00 | +00:32:00 |
| RedJ2045-0022    | 20:45:00 | -00:22:00 |
| RedJ2056+0032    | 20:56:00 | +00:32:00 |
| RedJ2113-0028    | 21:13:00 | -00:28:00 |
| RedJ2120-0020    | 21:20:00 | -00:20:00 |
| RedJ2320+0018    | 23:20:00 | +00:18:00 |
| RedJ2042-0039    | 20:42:00 | -00:39:00 |
| RedJ2203-0052    | 22:03:00 | -00:52:00 |
| RedJ2048+0056    | 20:48:00 | +00:56:00 |
| BrightJ2036+0038 | 20:36:00 | +00:38:00 |
| BrightJ2323+0057 | 23:23:00 | +00:57:00 |
| BrightJ2103-0043 | 21:03:00 | -00:43:00 |
| BrightJ2241-0103 | 22:41:00 | -01:03:00 |
| BrightJ2259+0103 | 22:59:00 | +01:03:00 |
| BrightJ2043+0045 | 20:43:00 | +00:45:00 |

**Table 2.3:** The target coordinates

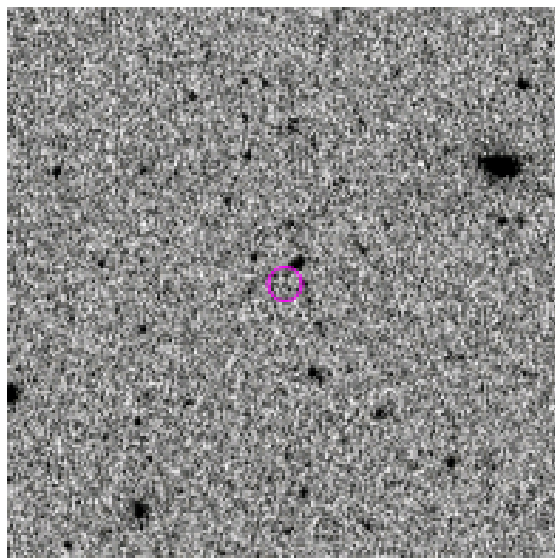


**Figure 2.2:** The finding chart of quasar RedJ0000+0032, as seen in the r-band of SDSS (DR7). The purple circle shows the position of the target in the field.

## 2.3 FRAME PROCESSING

The direct image that we get from a telescope contains multiple instrumental features. The aim of image processing is to reduce the image obtained with the telescope (raw image) and rebuild the original signal to the final processed image (science image), that is corrected for these errors and can be used for scientific measurements. For this purpose, calibration frames are obtained and various imperfections are taken into account. The scripts that are used for all the data reduction processes and extraction of the spectra can be found in <https://github.com/LigeiaR/Data-Reduction>.

### 2.3.1 BIAS FRAMES

Because of the readout noise (RON) of the CCD (Charged-Coupled-Device), in an astronomical image we do not have the same number of counts per pixel. Instead, the pixel values follow a Gaussian distribution with a mean of counts and a standard deviation given by the readout noise. This means that some pixels, that receive no light, get negative values. To avoid having negative values in the output image, an electronic data offset value is given by the CCD during readout. As a result, even if there are unexposed pixels, there is always some charge present. However, this is an artificial level and not an actual measurement of light. Therefore, this bias level needs to be removed from the raw images. For this pur-

pose, a number of bias frames are taken and are averaged to create a master bias frame. Bias frames are zero second time exposures and are taken when the shutter of the telescope is closed. Creating a master bias, that is a representative of the variations of the bias level in the detector field, reduces the impact of the readout noise in the master bias and gives a more accurate estimate of the bias level. The master bias is then removed from the raw image.

To create a master bias, 44 bias frames are combined with the IRAF<sup>1</sup> task `imcombine`, using the python script `mkspecbias`. Combining parameters `median` and `avsigclip` are used. The former is a combination method, with median being better at avoiding outliers than other options, while the latter is a rejection method and rejects pixels using average sigma clipping.

Furthermore, the frames are inspected for overscan regions, which are rows and columns on the edge of the frames that are not exposed to light. Thus, overscan regions contain only the bias level and need to be removed. For this, the median of the overscan region is computed and is then subtracted from the rest of the pixels of the image.

### 2.3.2 FLAT FIELD CORRECTION

Each pixel of the CCD has a different quantum efficiency with respect to the incoming radiation. A result of these pixel-to-pixel variations is that the raw image is not an accurate representation of the actual light distribution of the source, but a distribution of unequal quantum efficiencies. As a result, the raw images need to be corrected for these variations and for this purpose flat field frames are used. Flat fields are images of a uniform illuminating source, and for spectroscopy, dome flats are used.

For this analysis, 15 halogen lamp flat frames are combined using the python script `mkspecflatg4s1`, in order to create a master flat. Flat frames also contain a bias level, so the master bias is subtracted from the flat field frames and then the master flat is created.

Furthermore, the master flat needs to be normalized, which results to a final frame with average mean pixel values close to 1. To normalize the master flat, we divide by the mean pixel value of the uniform flat field. The flux of each pixel (i,j) in the master flat can be written as,

$$F_{ij} = \alpha_{ij}F, \quad (2.1)$$

where  $F$  is the mean flux of the uniform flat field, and  $\alpha_{ij}$  describes the pixel-to-pixel variations. By normalizing (dividing by  $F$ ), we get an image that represents

---

<sup>1</sup>Image Reduction and Analysis Facility, a general purpose software system for the reduction and analysis of astronomical data. IRAF is written and supported by the National Optical Astronomy Observatories (NOAO) in Tucson, Arizona.

the pixel-to-pixel variations. The flux of each pixel in the raw image can be written as,

$$G'_{ij} = \alpha_{ij}G_{ij}, \quad (2.2)$$

where  $G_{ij}$  is the actual flux that falls on each pixel. So, dividing by the normalized flat field ( $\alpha_{ij}$ ), we get the image containing the actual flux falling on each pixel, reconstructing thus the original signal of the source.

### 2.3.3 COSMIC RAY CORRECTION

Astronomical images include cosmic ray hits, affecting the quality of the image and the further spectroscopic analysis. Thus, another important step of image processing is cosmic ray removal.

First, the two exposures of each spectrum are combined, providing an initial phase of correction, because usually cosmic rays do not affect all the exposures. Since, only two exposures of the same object are taken, the probability of a cosmic ray hitting the same pixel is higher than if there were multiple exposures. So, further processing is required to make sure all cosmic rays are removed.

The data are then corrected using the algorithm `lacos_spec` [van Dokkum \(2001\)](#), with a detection limit for cosmic rays `sigclip= 4.5` and the algorithm is applied iteratively with a maximum number of iterations `niter=3`, using the IRAF script `prepare2`. Cosmic rays are distinguished from other objects by their arbitrary size, and are chosen based on Laplacian edge detection (sharpness of their edge). After the pixels that are hit by cosmic rays are selected, the algorithm interpolates their values from neighbouring "good" pixels (replacing them by the median).

The two bias subtracted, flat and cosmic ray corrected frames of each object are then combined to achieve a better quality spectrum extraction. The raw spectrum obtained from the telescope and the final bias, flat field and cosmic ray corrected spectrum is shown in [Figure 2.4](#).

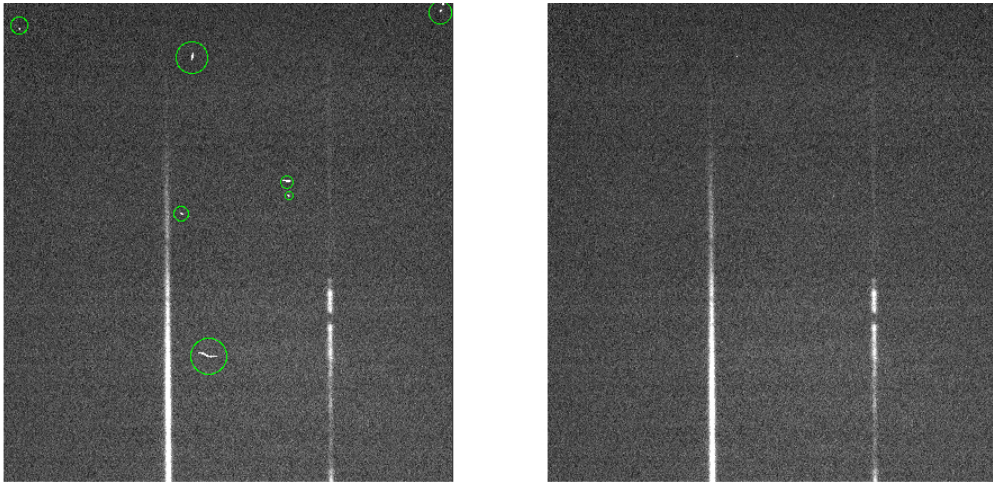


**Figure 2.3:** Part of the spectrum of RedJ0000+0032 before (left) and after (right) the cosmic ray correction algorithm is applied. Cosmic rays are seen inside the green circles in the left figure.

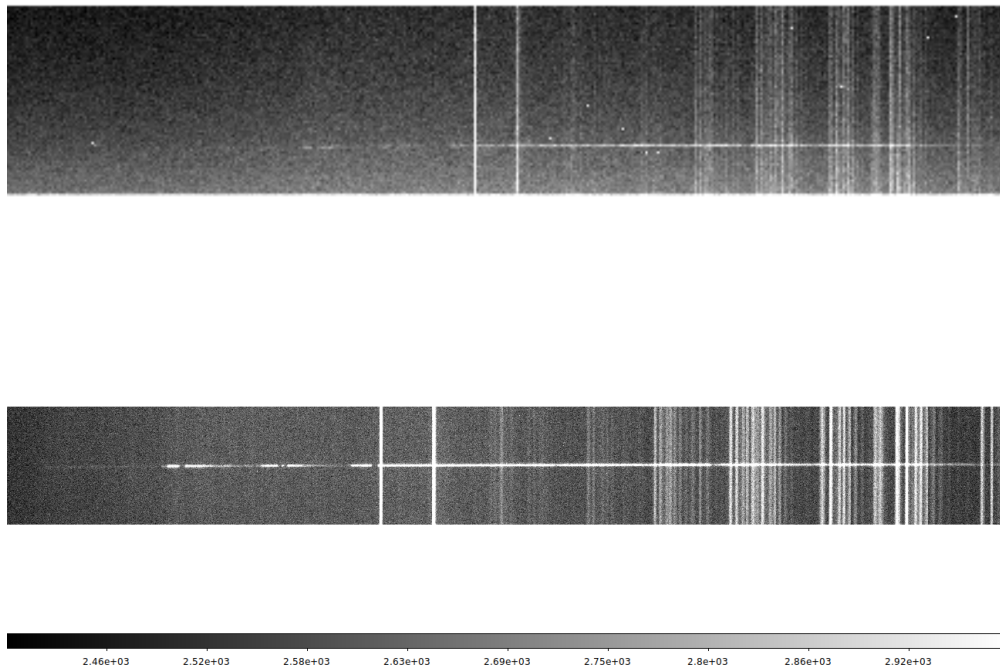


**Figure 2.4:** *Upper panel:* The raw spectrum of quasar RedJ0000+0032. *Lower panel:* The bias, flat field and cosmic ray corrected quasar spectrum. The spectrum is  $90^\circ$  rotated.

## 2.4 EXTRACTION OF THE SPECTRA

The extraction of the spectrum is done using the IRAF script `extract1`. First, `hedit` is used to set the dispersion axis in the header along rows (`DISPAXIS=1`). The script uses the task `apall`, which is run interactively, allowing for defining apertures around the object and tracing of the 2D spectrum, as seen in Fig. 2.5. Variance weighted optimal extraction is performed, so that different weights are given to different parts of the spectrum and average background subtraction is done after defining the background regions around the object. After this procedure the 1D spectrum is extracted.

### 2.4.1 WAVELENGTH CALIBRATION

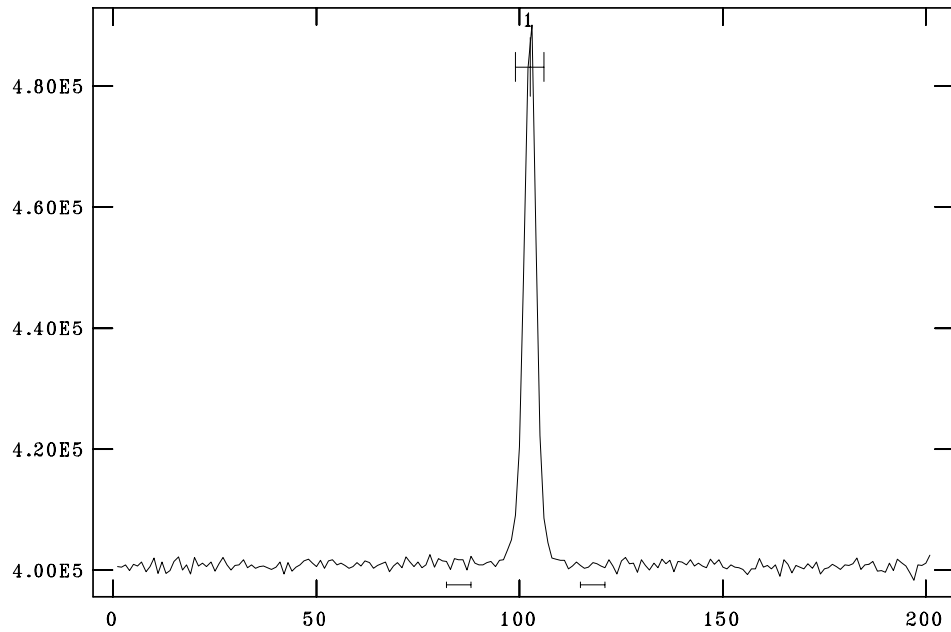
At this stage the dispersion axis of the spectrum needs to be converted from pixels (x,y) to wavelength. The procedure of assigning each pixel of the dispersion axis to the corresponding wavelength, using arc lamps, is called wavelength calibration. In this case, HeNe arc lamps were obtained immediately before each target observation. The arc frames contain emission lines of known wavelengths. Therefore, after identifying these lines and calibrating the arc spectrum, this can be used as a comparison for wavelength calibration of the quasar spectra.

For this purpose, the IRAF task `identify` is used, applying a 6th order Chebyshev polynomial. The emission lines are identified using the ALFOSC arc maps<sup>2</sup> for He and Ne of grism #4. The result of identify is seen in Fig. 2.6. Lines are identified throughout the whole spectrum range, with the shortest wavelength line being  $\lambda 3889\text{\AA}$  and the longest  $\lambda 8591\text{\AA}$ . Then the wavelength calibration function is applied to the spectrum with the task `dispcor`, i.e, a wavelength is associated to each pixel. The wavelength calibration done on the arc, is then used to calibrate the science spectra. To evaluate the wavelength calibration the plot of the residuals needs to be assessed. Since the dispersion for grism #4 is  $3.3\text{\AA}/pix$  and the root mean square (rms) is  $rms=0.32\text{\AA}$ , the accuracy achieved is  $10^{-1}$  of the pixel, which is a good result. Also, the points are randomly scattered around zero and there is no significant trend for concentration.

---

<sup>2</sup><http://www.not.iac.es/instruments/alfosc/lamps/>

NOAO/IRAF V2.16.1 christina@christina-Lenovo-G50-70 Mon 22:48:29 10-Dec-20  
 Image=spek1, Sum of columns 1125-1274  
 Define and Edit Apertures



NOAO/IRAF V2.16.1 christina@christina-Lenovo-G50-70 Mon 12:45:08 24-Sep-20  
 func=legendre, order=4, low\_rej=3, high\_rej=3, niterate=0, grow=0  
 total=166, sample=166, rejected=0, deleted=14, RMS=0.08972  
 Aperture 1 of spek1

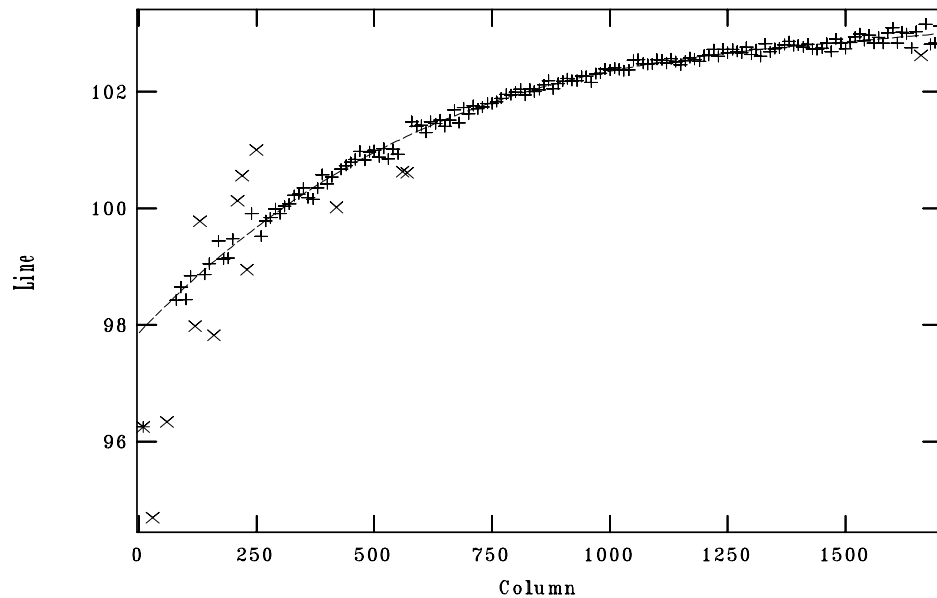


**Figure 2.5:** *Top panel:* Defining and editing the apertures around the object RedJ0000+0032, and the background regions around the object. *Bottom panel:* Tracing of the RedJ0000+0032 2D spectrum, where 14 deviating points have been deleted to achieve an rms of 0.0897 Å.

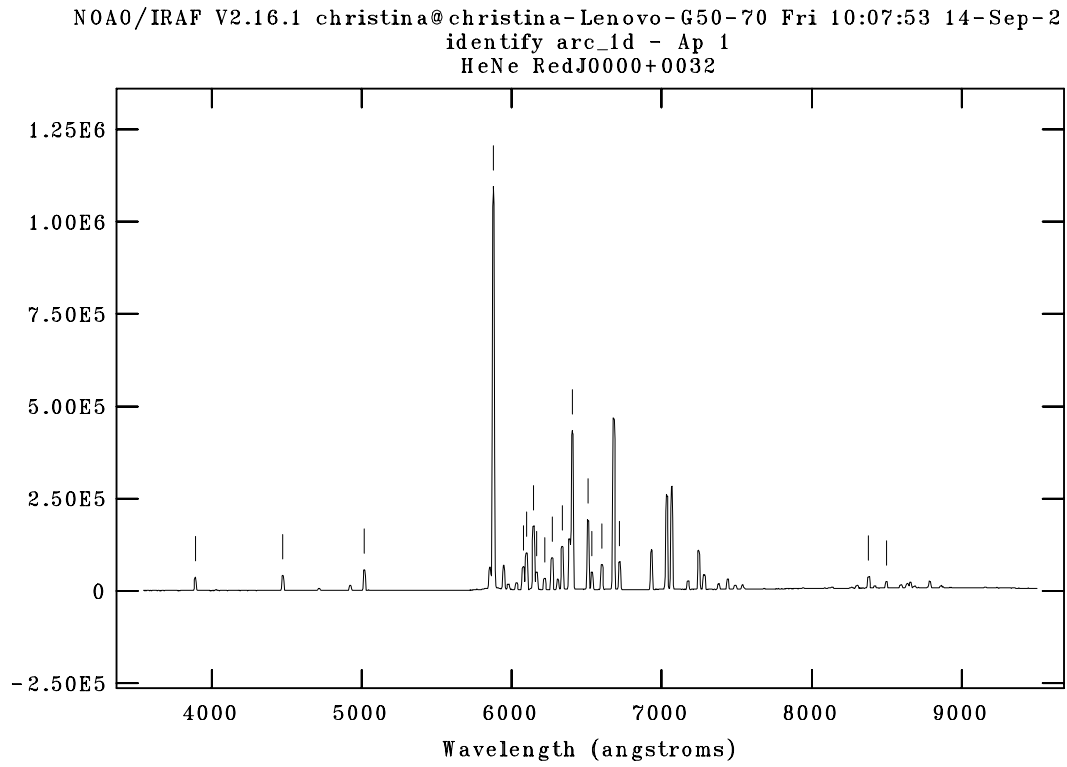


**Figure 2.6:** The identified throughout the wavelength range of the spectrum

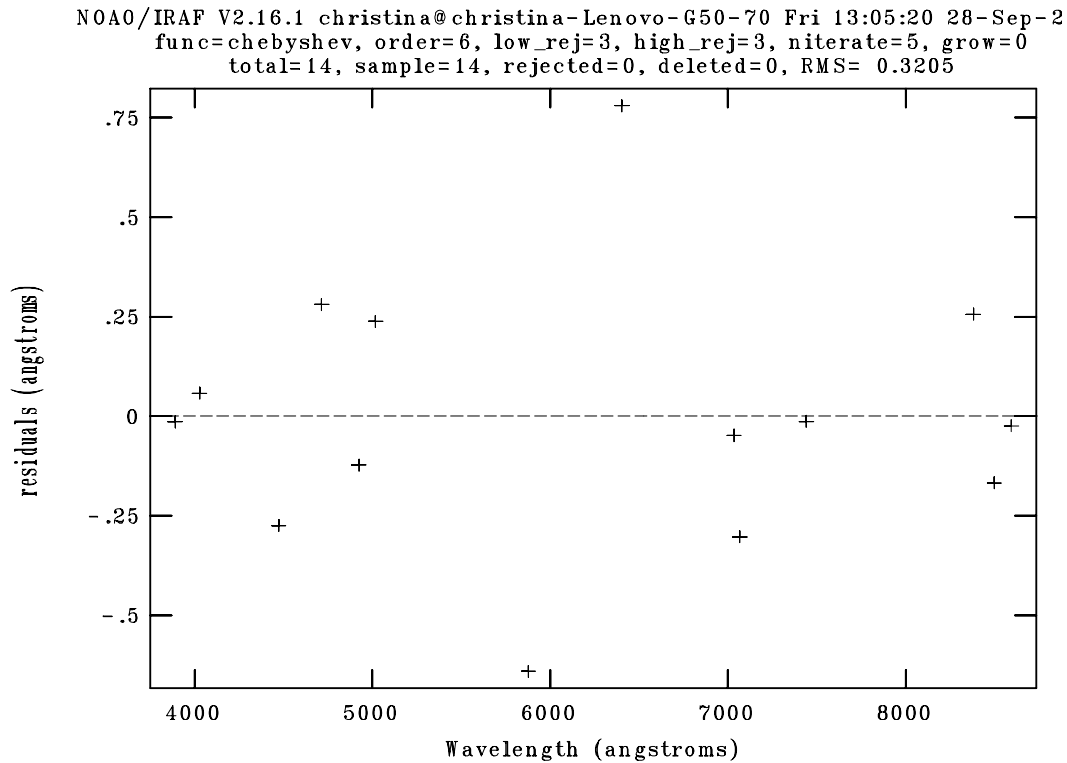


**Figure 2.7:** The residual plot for the standard star observed with the 1.3" slit. The best fit is obtained with a 6th order Chebyshev polynomial giving an rms of  $0.3205\text{\AA}$ , and points well spread around zero.

#### 2.4.2 FLUX CALIBRATION

Finally, the spectra are flux calibrated using the corresponding standard star of the same telescope setup as the science frames. The spectral flux of the standard stars is known, therefore they are used to determine the system sensitivity as a function of wavelength for all the apertures. This is done with the tasks `standard`, `sensfunc` and `calibrate`. `Standard` is producing a file containing calibration information, which is used by `sensfunc` to compute the calibration factor for each point and generate the sensitivity function, as a function of wavelength. Atmospheric extinction corrections are also applied. Then, the sensitivity function is applied to the data with the task `calibrate`, which converts the units of the flux to  $\text{erg s}^{-1}\text{cm}^{-2}\text{\AA}^{-1}$ .

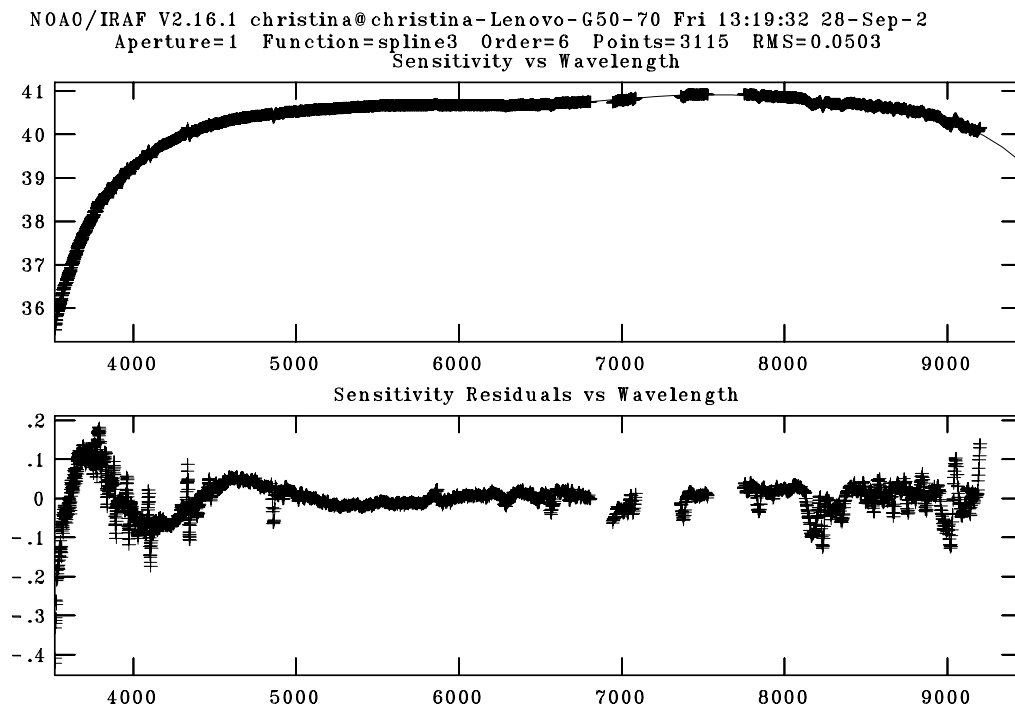


**Figure 2.8:** The sensitivity as a function of wavelength (top) and the sensitivity residuals as a function of wavelength (bottom). The sensitivity curve is well defined by an order 6 spline3 function with  $\text{rms}=0.0503\text{\AA}$ .

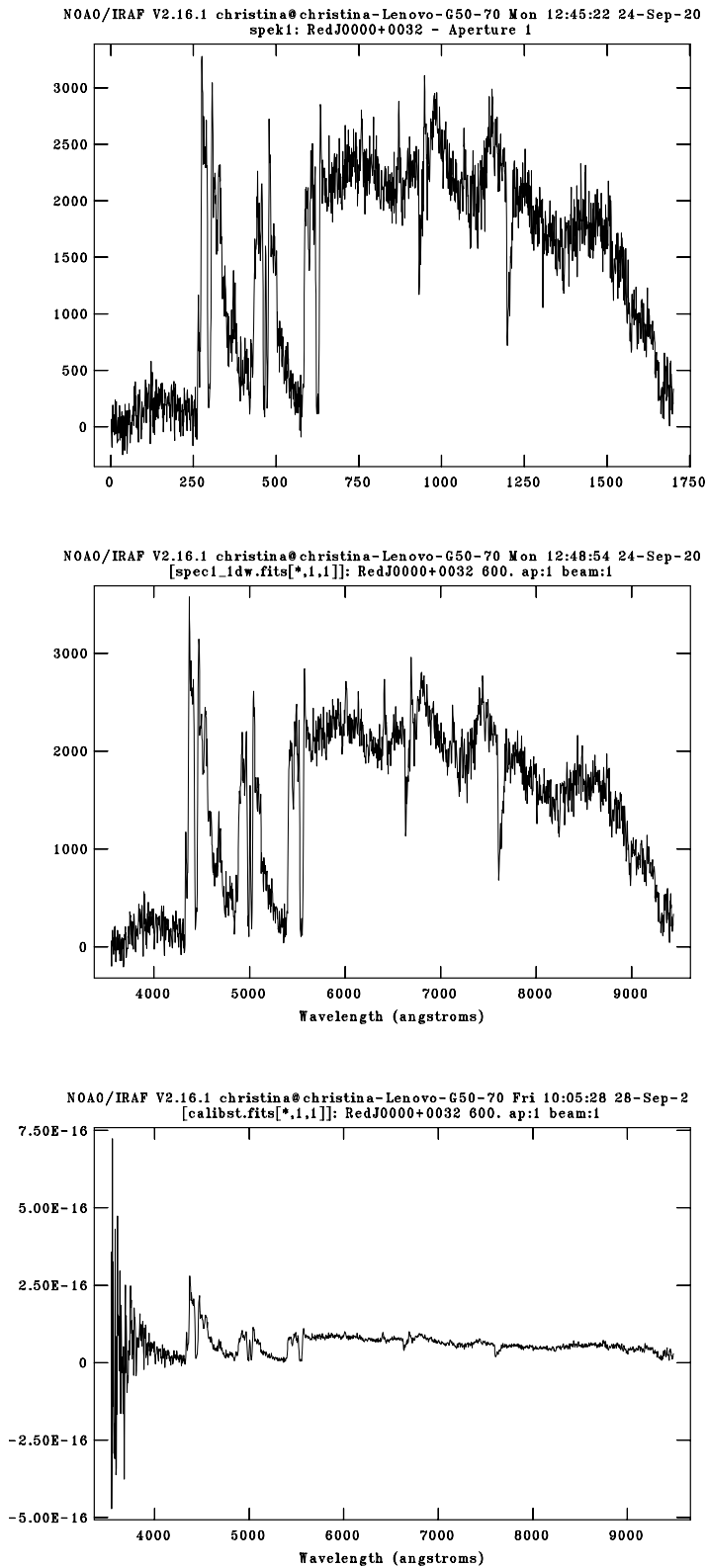


**Figure 2.9:** *Top figure* The raw spectrum of RedJ0000+0032. *Middle figure* The spectrum of RedJ0000+0032 after wavelength calibration. *Bottom figure* The final wavelength and flux calibrated spectrum of RedJ0000+0032.

# 3 RESULTS

## 3.1 SPECTROSCOPIC ANALYSIS

The complete list of the classified targets along with the calculated redshift  $z$  and their reddening,  $A_B$  is presented in Table 3.2. The redshift of the quasars was determined by visually identifying a prominent emission line in the spectrum of each target and simply overplotting the composite quasar template obtained by (Selsing et al., 2016). The composite spectrum is constructed using luminous blue QSOs at  $1 < z < 2.1$  selected from SDSS. Knowing the rest wavelength ( $\lambda_0$ ) of the elements and measuring their shifted wavelengths ( $\lambda$ ), the redshift  $z$  can be trivially calculated from

$$z = \left( \frac{\lambda}{\lambda_0} \right) - 1 \quad (3.1)$$

Using the calculated redshift, more lines are identified and visually confirmed by fitting the composite template. The extinction  $A_B$  is also visually determined by the fit. Finally, the reddened composite template (see Section 3.2) is overplotted along with the photometric data points of the SDSS and UKIDSS  $u, g, r, i, z, Y, J, H, Ks$  bands. All the spectra are scaled to the photometric r-band from SDSS, to achieve better flux calibration and avoid slit losses. Also, all spectra and composite templates (with and without reddening) are normalized to the wavelength range 5700-6600 Å. This way a better representation of the spectrum is achieved, since points that appear blueward of Ly- $\alpha$  and any other areas with strong absorption are excluded.

An example of the fitting procedure is shown in Figure 3.1, where the red quasar RedJ2048+0056 is plotted. The redshift is calculated ( $z=2.37$ ) by identifying the CIV emission line. Visible are mainly the emission lines Ly- $\alpha$ , CIII and SiIV. The reddening is low with  $A_B = 0.4$  and both the reddened and unreddened composite templates match the observed spectrum well. This is a typical quasar spectrum,

with most of the emission lines visible. The rest ( $\lambda_0$ ) and redshifted ( $\lambda$ ) wavelengths of the emission lines of RedJ2048+0056 are presented in Table 3.1.

| Species      | $\lambda_0$ [Å] | $\lambda$ [Å] |
|--------------|-----------------|---------------|
| Ly- $\alpha$ | 1215.24         | 4092.38       |
| SiIV         | 1397.61         | 4715.50       |
| CIV          | 1548.00         | 5214.00       |
| CIII         | 1908.73         | 6429.93       |

**Table 3.1:** The wavelengths of the emission lines identified in the spectrum of the quasar RedJ2048+0056. The redshift is found to be  $z=2.37$  from CIV.

| Target name      | Type    | $z$  | $A_B$ |
|------------------|---------|------|-------|
| RedJ0000+0032    | QSO     | 2.60 | 0.2   |
| RedJ2047+0045    | QSO     | 2.29 | 0.0   |
| RedJ0312+0035    | QSO     | 1.28 | 1.1   |
| RedJ0312+0032    | QSO     | 1.25 | 0.5   |
| RedJ2045-0022    | QSO     | 1.15 | 0.4   |
| RedJ2056+0032    | QSO     | 1.98 | 1.2   |
| RedJ2113-0028    | QSO     | 2.48 | 0.0   |
| RedJ2120-0020    | QSO     | 1.52 | 0.6   |
| RedJ2320+0018    | M-Dwarf | 0.00 | 0.0   |
| RedJ2042-0039    | QSO     | 2.36 | 0     |
| RedJ2203-0052    | QSO     | 1.25 | 0.4   |
| RedJ2048+0056    | QSO     | 2.37 | 0.4   |
| BrightJ2036+0038 | QSO     | 0.79 | 0.0   |
| BrightJ2323+0057 | QSO     | 2.73 | 0.4   |
| BrightJ2103-0043 | QSO     | 2.15 | 0.0   |
| BrightJ2241-0103 | QSO     | 1.12 | 0.0   |
| BrightJ2259+0103 | QSO     | 1.29 | 0.0   |
| BrightJ2043+0045 | QSO     | 2.46 | 0.0   |

**Table 3.2:** The spectroscopically identified targets.

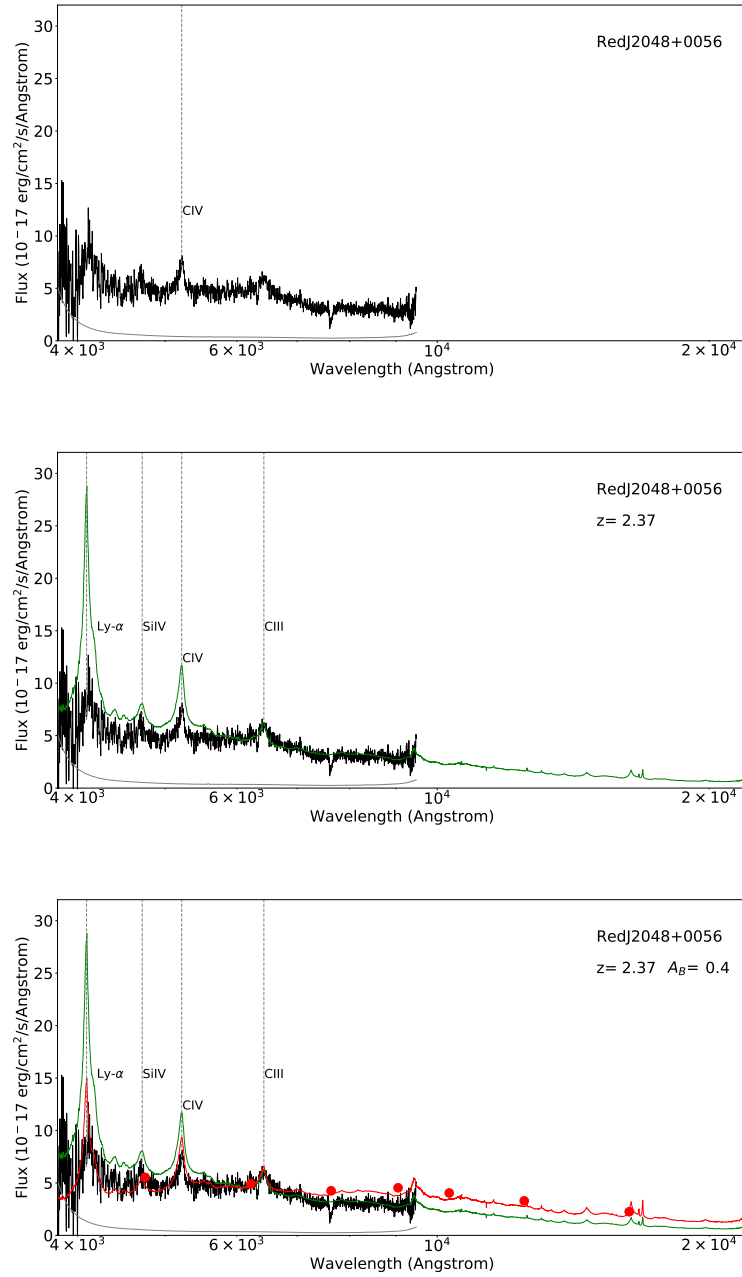


**Figure 3.1:** The figures show the spectrum of the red quasar RedJ2048+0056 and the plotting procedure that was followed. The upper figure shows the spectrum and the CIV emission line from which the redshift was determined. The middle figure shows the rest of the identified emission lines and the fitted composite spectrum (green line). The bottom figure shows the resulting spectrum after fitting the reddened composite quasar template from [Selsing et al. \(2016\)](#) (red line). The red dots are the photometric data points of the u,g,r,i,z,Y,J,H,Ks bands, from SDSS and UKIDSS. In the upper right corner of the figures the name of the target, the redshift and amount of reddening are listed.

### 3.2 DUST REDDENING

The reddening corrections and plotting of all the spectra are done using the python code *allspec.py*, which can be found in <https://github.com/LigeiaR/allspec/blob/master/allspec.py>.

The spectra are obtained through ground-based observations, which means that they are affected by Milky Way dust, that lays on the line-of-sight between the observer and the target. Intervening Milky Way dust alters the observed flux of the spectra. Thus, in order to obtain the original flux of the targets, Galactic extinction correction needs to be applied to all the spectra as well as the photometry. The estimation of Galactic extinction is done with the use of the SFD dust maps [Schlegel et al. \(1998\)](#) and taking into account the colour excess ( $E_{B-V}$ ) values. The  $E_{B-V}$  value of each target, is an indication of the amount of dust and is calculated by applying the SFD maps to the corresponding Galactic coordinates of each target.

The quasars are also dust-rich systems and reddening by intrinsic dust also occurs. To correct for this, the reddened composite template is also modeled according to the Small Magellanic Cloud (SMC) extinction, using the parametrization of the SMC extinction curve by [\(Pei, 1992\)](#). The fitting function covering all wavelengths is

$$A_\lambda = A_0 + \sum_{i=1}^6 \frac{a_i}{\left(\frac{\lambda}{\lambda_i}\right)^{n_i} + \left(\frac{\lambda_i}{\lambda}\right)^{n_i} + b_i}, \quad (3.2)$$

where  $A_\lambda$  is the total extinction,  $A_0$  is the flux of the composite spectrum in microns (rest-frame) scaled to zero. Taking into account the extinction  $A_B$

$$F_{AB} = A_\lambda \cdot A_B \quad (3.3)$$

and finally we get the model of the flux of the reddened composite spectrum as

$$model = (10^{-0.4 \cdot F_{AB}}) \cdot F_c, \quad (3.4)$$

where  $F_c$  is the flux of the composite spectrum (unreddened) in microns.

The extinction curve parameters  $a_i$ ,  $\lambda_i$ ,  $b_i$ ,  $n_i$  and  $K_i$  are listed in [Table 3.3](#).

As mentioned above, the spectra are scaled to the SDSS r-band, and in order to do so the r-band given in magnitudes is converted to flux using

$$F_r = 10^{0.4(-48.6-r)} \cdot \frac{3 \cdot 10^{18}}{\lambda_r} \quad (3.5)$$

| Small Magellanic Cloud |       |                    |       |       |       |
|------------------------|-------|--------------------|-------|-------|-------|
|                        | $a_i$ | $\lambda_i[\mu m]$ | $b_i$ | $n_i$ | $K_i$ |
| BKG                    | 185.  | 0.042              | 90.   | 2.0   | 2.89  |
| FUV                    | 27.   | 0.08               | 5.50  | 4.0   | 0.91  |
| 2175 Å                 | 0.005 | 0.22               | -1.95 | 2.0   | 0.02  |
| 9.7 $\mu m$            | 0.010 | 9.7                | -1.95 | 2.0   | 1.55  |
| 18 $\mu m$             | 0.012 | 18.                | -1.80 | 2.0   | 2.89  |
| FIR                    | 185.  | 0.030              | 25.   | 0.00  | 1.89  |

**Table 3.3:** The SMC extinction curve parameters used to correct for reddening. BKG, FUV and FIR represent the background, far-ultraviolet and far-infrared extinction respectively, while the others represent the 2175Å, 9.7 $\mu m$  and 18 $\mu m$  extinction features. (Pei, 1992)

### 3.3 THE RED QSO SPECTRA

In Figure 3.4 the spectra of the 11 red quasars are shown as well as the spectrum of the M-dwarf. Two of the red quasars are BAL QSOs (RedJ0000+0032 and RedJ2042-0039) accounting for 18% of the sample. Most spectra show a good fit between spectrum and photometry in the blue end, while there is a poor fit of the photometry beyond  $\sim 5900$  Å. The reason is that this part of the spectrum suffers from second order contamination, an effect that is noticeable in grism #4 of ALFOSC, which was used for all the observations. Second order contamination usually takes place in low resolution spectra, taken in the first diffraction order. The effect could have been corrected by either using a blue light blocking filter, which would result in loss of the blue part of the spectrum or by using two different spectrograph settings, which would significantly increase the exposure times. Since very high spectrophotometric accuracy is not necessary for this work, the effect is not corrected.

Quasar **RedJ0000+0032** is the most distant of the sample, with a redshift of  $z=2.60$ , estimated by a strong Ly- $\alpha$  emission line. Under the assumption of Friedmann-Lemaître-Robertson-Walker metric and the Hubble parameter at a given redshift  $H(z) = H_0 E(z)$  the proper distance can be expressed as

$$d_P(z) = \frac{c}{H_0} \int_0^z \frac{dz}{E(z)}, \quad (3.6)$$

where  $z$  is the redshift,  $H_0$  is the Hubble constant,  $c$  is the speed of light and  $E(z)$  is given by equation 1.2. Following the above equations the distance of RedJ0000+0032 is calculated as  $d = 6 \cdot 10^6$  kpc, which corresponds to  $\sim 10^4$  the distance between the Milky-Way and Andromeda (MW-Andromeda distance=778 kpc).

Identified are the emission lines CIII, CIV, SiIV, OI and OIV. This quasar is dominated by high ionization species, like CIV, SiIV and OIV and is characterized by low reddening with  $A_B = 0.2$ . It is seen that the composite spectrum before and after the SMC reddening almost match. In this case, the reddening is caused by the BAL regions and not by intervening clouds along the line-of-sight. Quasar **RedJ2056+0032** is the most reddened of the sample, with  $A_B = 1.2$ . The redshift is calculated as  $z=1.98$  from CIII. CIV and MgII emission lines are also identified. The composite spectrum before and after the reddening do not match, with the red line being noticeably higher in the red end of the spectrum, indicating the reddening of the quasar.

Quasars **RedJ2047+0045**, **RedJ2113-0028** and **RedJ2042-0039** have no reddening ( $A_B = 0$ ). RedJ2042-0039 is also a BAL QSO. CIII is the most clear line seen in emission, and thus is used for the calculation of the redshift. Ly- $\alpha$  is absorbed by the Ly- $\alpha$  forest, so the composite spectrum does not match the line and NV is seen in emission. Parts of SiIV and CIV are also absorbed by the BAL regions. Because the strong absorption is caused intrinsically by the BAL regions and not by intervening clouds this QSO has  $A_B = 0$ .

**RedJ2047+0045** and **RedJ2113-0028** show a poor fit with the template, since the emission lines are very faint, and as a consequence, they were the most non-trivial to identify.

**RedJ0312+0032** and **RedJ0312+0035** are pair quasars, with redshifts  $z=1.25$  and  $z=1.28$  respectively. The same emission lines are identified for both (MgII and CIII). RedJ0312+0035 is a relatively high reddened quasar ( $A_B = 1.1$ ), in contrast with its pair that has much lower reddening ( $A_B = 0.5$ ), and it is probably reddened by its own galaxy. The angular separation of the two quasars in the sky is calculated as

$$\theta = \cos^{-1}[\sin(DEC1) \cdot \sin(DEC2) + \cos(DEC1) \cdot \cos(DEC2) \cdot \cos(RA1 - RA2)], \quad (3.7)$$

where RA and DEC are expressed in degrees. Converted to arcseconds, the angular separation is  $\theta = 199.6$  arcsec. This corresponds to  $\sim 1715$  kpc, which is about twice the Milky Way-Andromeda distance. Consequently, the two quasars have a large angular separation in the sky, but low redshift difference (2%). It is unlikely

that the system is a result of gravitational lensing, since there is a significant difference seen in the emission lines of the spectra, i.e in the MgII emission line, which is the most apparent. In addition, there is no foreground dusty galaxy in the anticipated lens position - there is no visible DLA absorber. Their redshift difference is low, but still the redshifts are not identical, for the system to be considered a lens. More importantly, the separation of the two quasars is quite large. (Separations of 1"-3" are considered candidate lens systems). Thus, the pair is interpreted as a binary quasar. The comparison of the spectra of the two quasars is seen in Figure 3.2.

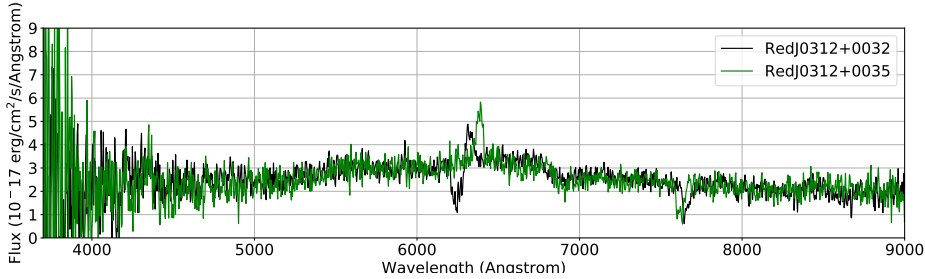


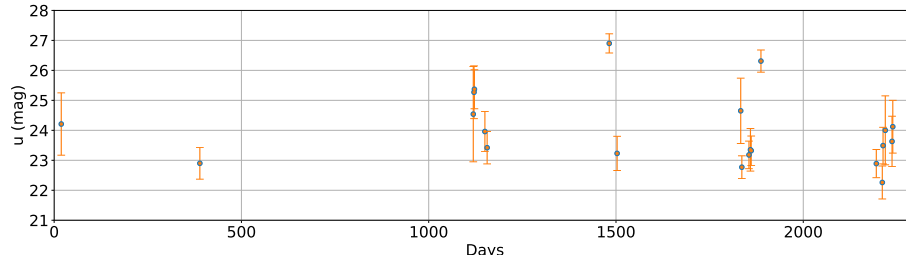
**Figure 3.2:** Comparison of the pair quasars spectra. The spectrum of RedJ0312+0032 is shown with the black line and the spectrum of RedJ0312+0035 is shown with green. The flux of RedJ0312+0032 has been rescaled to the flux range of RedJ0312+0035. It is seen that the two spectra differ in the MgII emission line. RedJ0312+0035 has stronger MgII emission, and the MgII line is more redshifted due to the higher redshift of RedJ0312+0035.

**RedJ2320+0028** is an early type M-dwarf star, based on the shape of its spectral energy distribution (SED). A strong sodium (Na) absorption line is visible which matches the spectrum to the M1-dwarf spectral template, while a faint Ha line matches it to the K type dwarf star template. The spectrum of RedJ2320+0028 peaks earlier than very cold red stars, so it is not a very cold star, which would justify its red colour. Instead, other reasons have to be explored to explain its reddening, which eventually led us to its selection. Those are:

- 1) The star is young and is still embedded in gas and dust, so its radiation is emitted in the infrared.
- 2) The star is close to a star-forming region.
- 3) The star is variable, causing it to show a K-excess.

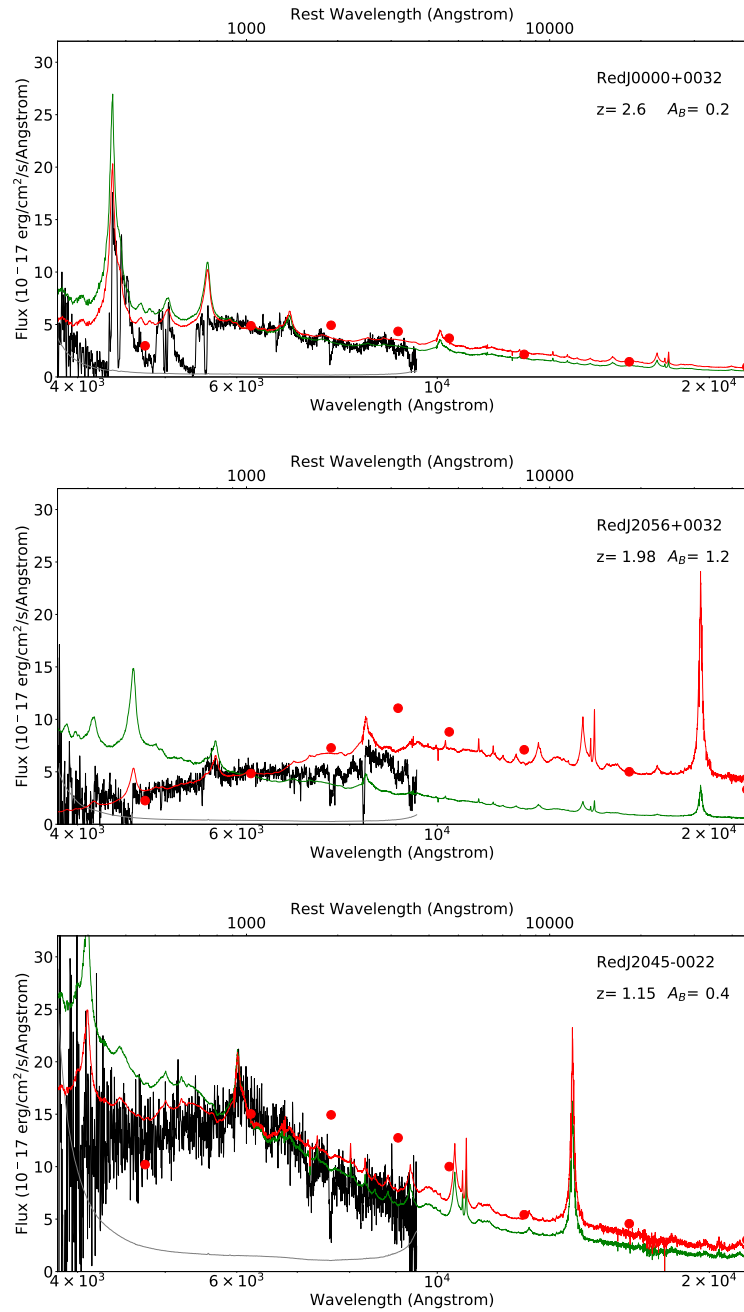
The star's variability is tested by reviewing its magnitudes from secondary SDSS observations during the years 1998-2004. Figure 3.3 shows the variability of the u band, which is the only magnitude that appeared to differ between observations. From the plot it is seen that the only magnitude values that depart

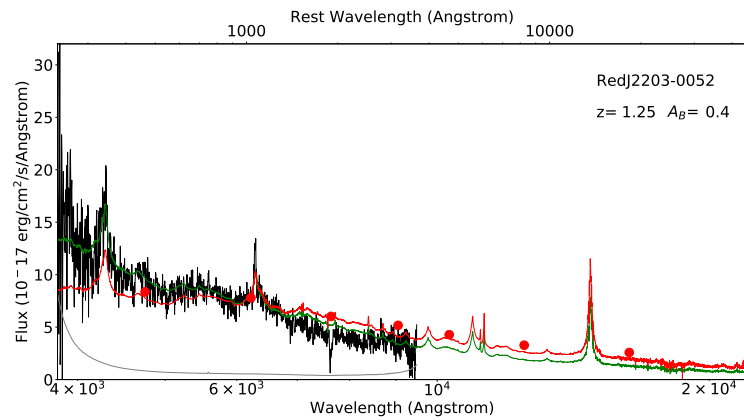
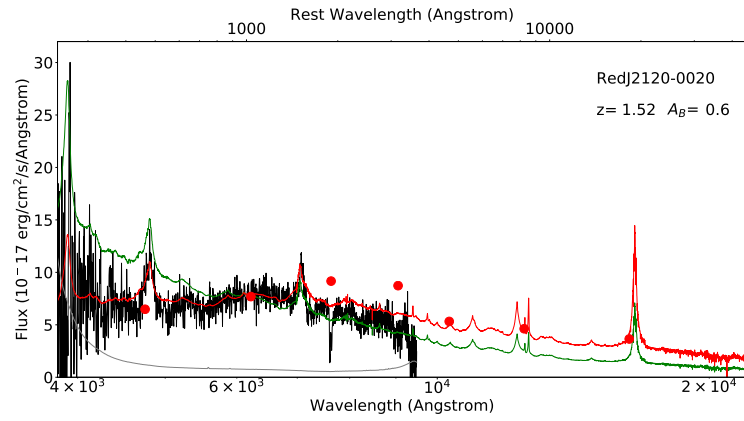
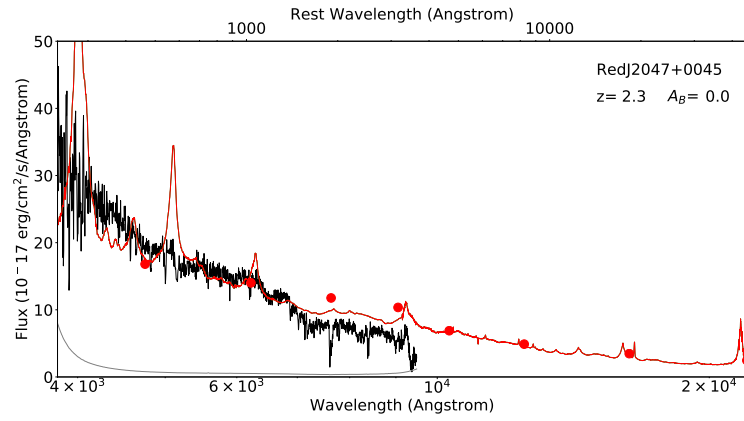
from the average are at  $u \sim 27$ . This observation, with an error bar that small, is considered non-reliable, since it is above the detection limit of SDSS. The other values do not appear to vary significantly, leading to the conclusion that the star is not variable.

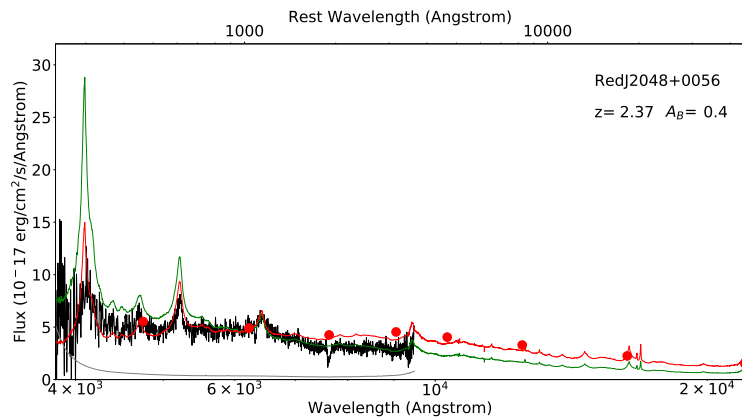
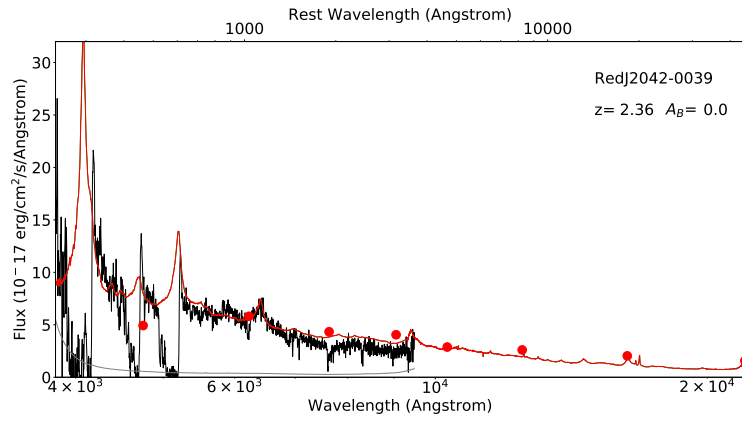
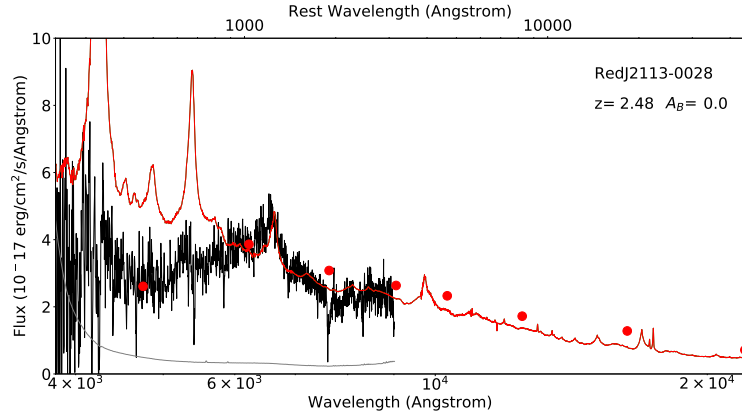


**Figure 3.3:** Variability plot of the SDSS u magnitude, with the corresponding error bars, over the period of 1998-2004 for the dwarf star RedJ2320+0028.

As a result, the star is considered a young M-dwarf that is still embedded in gas and dust or is close to a star forming region. This causes it to appear in the red, thus including it to our selection, and making it the only contaminant star of our sample.







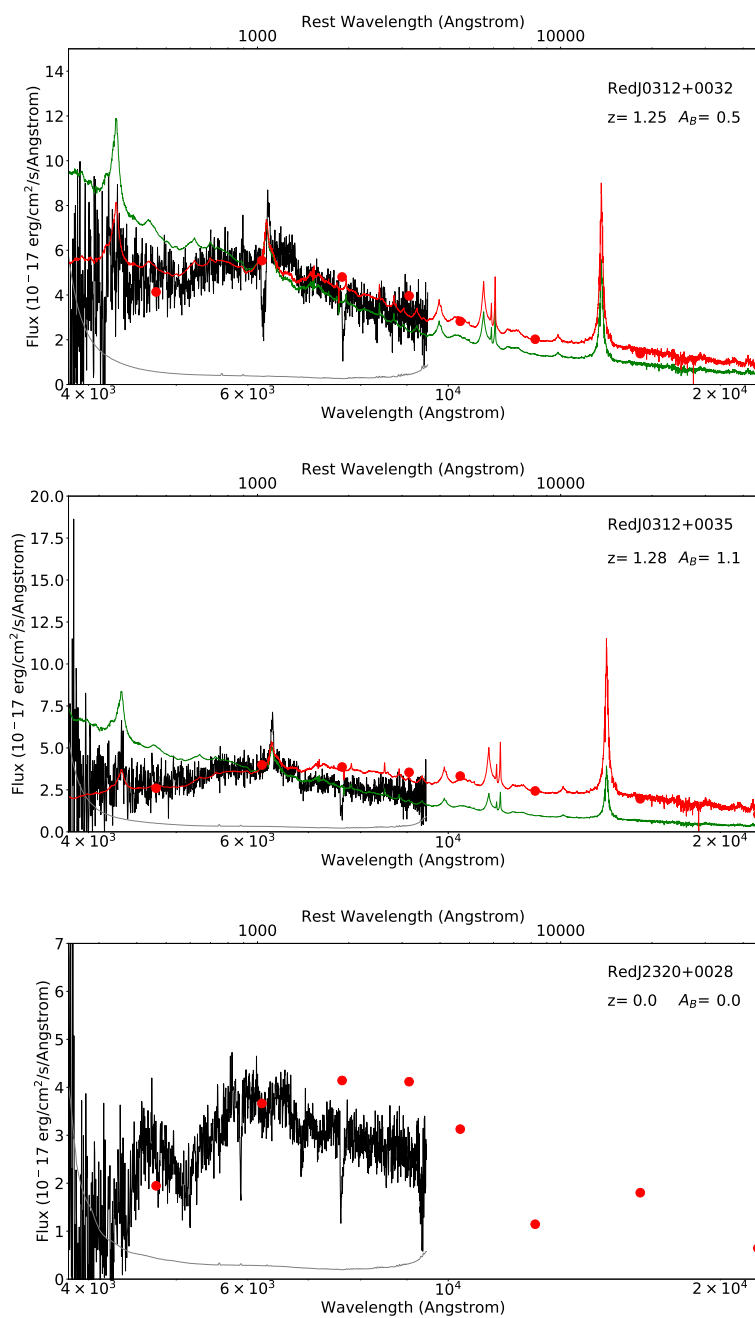


**Figure 3.4:** The spectra of all the observed red quasars. The M-dwarf star shown in the last figure.

### 3.4 COLOUR DIAGRAMS

To demonstrate the efficiency of our selection criteria, the quasar samples are visualized in colour space. This way the location of the different types of quasars with respect to other sources is made clear. The distribution of quasars is shown in the  $g-r$  vs.  $J-K_s$  plot (Figure 3.5), where it is clearly seen that red quasars deviate from the fundamental location of the normal bright QSOs, as well as from the stellar track. All the SDSS spectroscopically confirmed QSOs as well as the normal bright quasars observed at the NOT lie below the  $g-r > 1$  selection limit. This makes this cut important since it reveals a region poorly explored for red quasars.

Although BrightJ2323+0057 is at  $g-r < 1$ , it is the only normal bright QSO that enters the selection area for red quasars. This is the only BAL of the normal bright sample, and the only one that has some amount of reddening ( $A_B=0.4$ ), thus deviating from the normal bright quasar locus.

In addition, the M-dwarf from the NOT sample is far off the stellar track, showing a  $K_s$  excess and within our selection limits. As mentioned above the star is possibly young and embedded in dust and gas making it emit in the red, and as a result was falsely selected as a candidate red quasar. Out of the 162 previously spectroscopically confirmed quasars, 80 are within the redshift range  $1 < z < 2$ , a range that includes the peak of the quasar density. The least number of QSOs lie at higher redshifts ( $z > 3$ ). In fact, only 7 quasars are found in the redshift range  $3 < z < 10$ . This is because they become fainter with distance and more difficult to detect. Also, the space density of quasars at  $z > 3$  declines rapidly at high redshifts (Shaver et al., 1996). Low redshift quasars ( $0.05 < z < 1$ ) appear to have blue colours in  $g-r$ , but show a  $K_s$  excess (Figure 3.5).

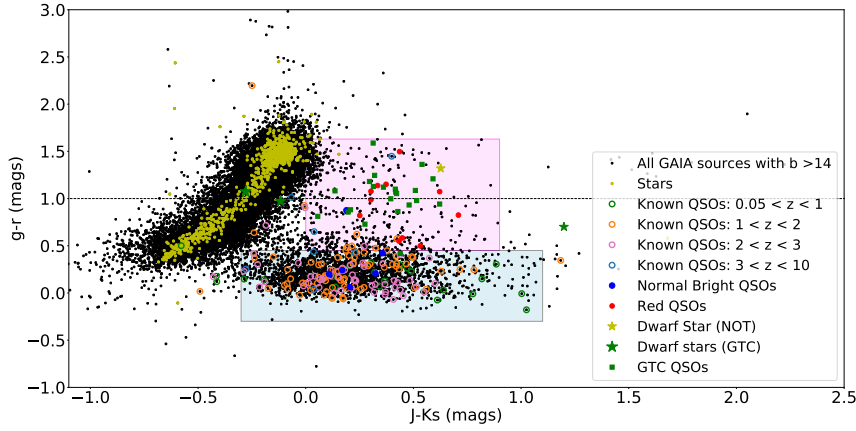


**Figure 3.5:** The Gaia sources with the complete quasar sample from NOT and GTC along with the already spectroscopically confirmed quasars from SDSS DR12 in  $g-r$  vs  $J-Ks$  colour space. The red quasars observed at the NOT are marked with red dots. The normal bright quasars (NOT) are the blue dots. The quasars observed at the GTC are shown with green cubes. The dwarf stars of the NOT and GTC samples are shown with yellow and green stars respectively. The yellow dots show the stellar track. The spectroscopically confirmed quasars at the redshift ranges  $0.05 < z < 1$ ,  $1 < z < 2$ ,  $2 < z < 3$  and  $3 < z < 10$  are shown with green, orange, pink and blue open circles respectively. The pink selection box shows the area, where the red quasars from the two samples are located, while the blue box shows where most of the normal bright quasars are located. The black dashed line shows our  $g-r$  selection cut.

The separation of quasars from stars is very well demonstrated in near-infrared/mid-infrared colour space, as seen in Figure 3.6. From the 162 spectroscopically confirmed QSOs, 145 lie at  $W1-W2 > 0.8$ , and this is consistent with our selection limit. The stellar track is seen below this cut, which makes this criterion important for rejecting stars from our sample. As illustrated in the bottom panel of Figure 3.6, only one MIR colour criterion ( $W1-W2$ ) is sufficient for isolating quasars from stars.

However, there are some SDSS QSOs in that region, mostly at  $z > 2$  and especially in the redshift range  $3 < z < 10$ . Included are two GTC targets, Gaia\_QSO\_1103+1325 and Gaia\_QSO\_1124+1342, at redshifts  $z=2.16$  and  $z=1.30$  respectively. In the NOT sample, two targets lie at  $W1-W2 < 0.8$ , the M-dwarf, as expected, and the normal bright QSO BrightJ2103-0043, with redshift  $z=2.15$ . The targets were selected, because the selection cut was loosened in order to include more candidates for observation. This resulted in contamination of my sample, with the M-dwarf, and indicates that the mid-infrared selection cut is very important for reducing stellar contamination of the sample and effectively selecting QSO candidates. As

seen in Figure 3.7, the  $W1-W2 < 0.8$  cut is a balance between high completeness and low contamination (Guo et al., 2018). The proper motion criterion has also been imposed. However, the M-dwarf is located at a distance of  $d=1084$  kpc (MW-Andromeda distance = 778 kpc), and as a result, is far enough to fall within the  $3\sigma$  proper motion criterion, and be selected.

According to these, by combining the SDSS spectroscopically confirmed quasars, the NOT and GTC samples, the calculated completeness of quasars at  $W1-W2 > 0.8$  is 90.6 %, while the contamination by stars is only 1.6 %.

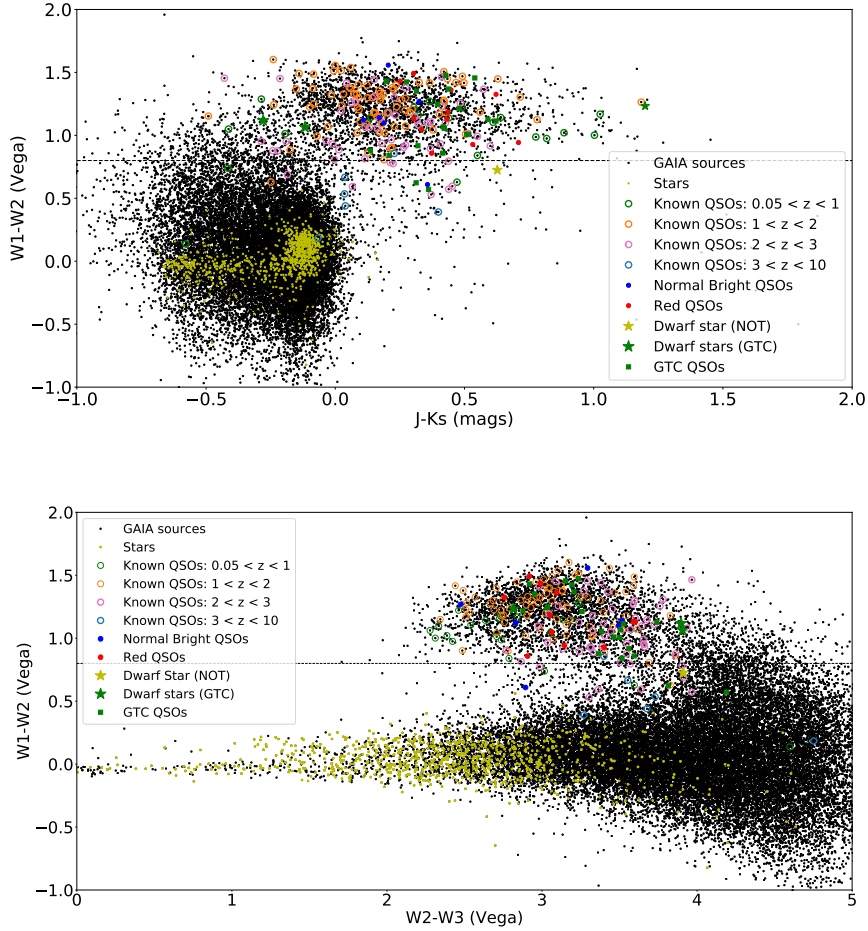


**Figure 3.6:** The  $W1-W2$  vs.  $J-Ks$  (Top figure) and  $W1-W2$  vs.  $W2-W3$  (Bottom figure) colour diagrams showing the quasar distribution in NIR and MIR colour space. The  $W1-W2 > 0.8$  MIR selection limit is shown with a black dashed line.

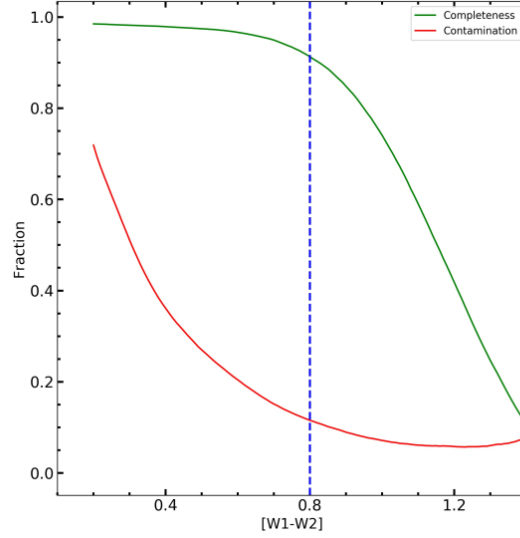


**Figure 3.7:** Quasar completeness (green curve) and stellar/galactic contamination (red curve) as a function of W1-W2. The blue dashed line shows the W1-W2 cut at W1-W2=0.8. Taken from Guo et al. (2018).

It is interesting to see where the BAL QSOs are located in colour space depending on the reddening and redshift. This is illustrated in Figure 3.8, where all the sources from the NOT and the GTC samples are seen in NIR/MIR and MIR colour space, colour coded according to reddening and redshift. As seen in the upper left panel of Figure 3.8, BAL QSOs have low reddening, while only 33.3 % of them are at  $g-r > 1$ . This shows that a lower  $g-r$  limit can introduce more BALs in the sample. The dashed selection box shows the location of all the normal bright QSOs, excluding the normal bright BAL that departs from this region. It is notable that all the normal bright QSOs have zero reddening, while the normal bright BAL has  $A_B = 0.4$ , and as a result it appears redder in the  $g-r$  plane. In general, there is a trend for increasing reddening in the  $g-r$  plane.

The upper right panel of Figure 3.8 shows all the sources in NIR/MIR space colour coded according to the redshift. It is seen that most of the BALs have high redshift. As the pink crosses indicate, three high redshift QSOs have zero reddening, one of which is a BAL in the NOT sample (absorption caused intrinsically by the BAL region). All the BALs at  $g-r > 1$  have high redshift, while lower redshifts are observed generally in the blue regions of the plot.

The lower panels of Figure 3.8 show the position of BALs in MIR colour space. It is seen that 83.3 % of the BALs are at  $W1-W2 > 0.8$  (only 2 GTC BALs are below the selection limit). High redshift BALs are seen in the  $W1-W2$  region between 0.8 and 1.3 Vega mags.

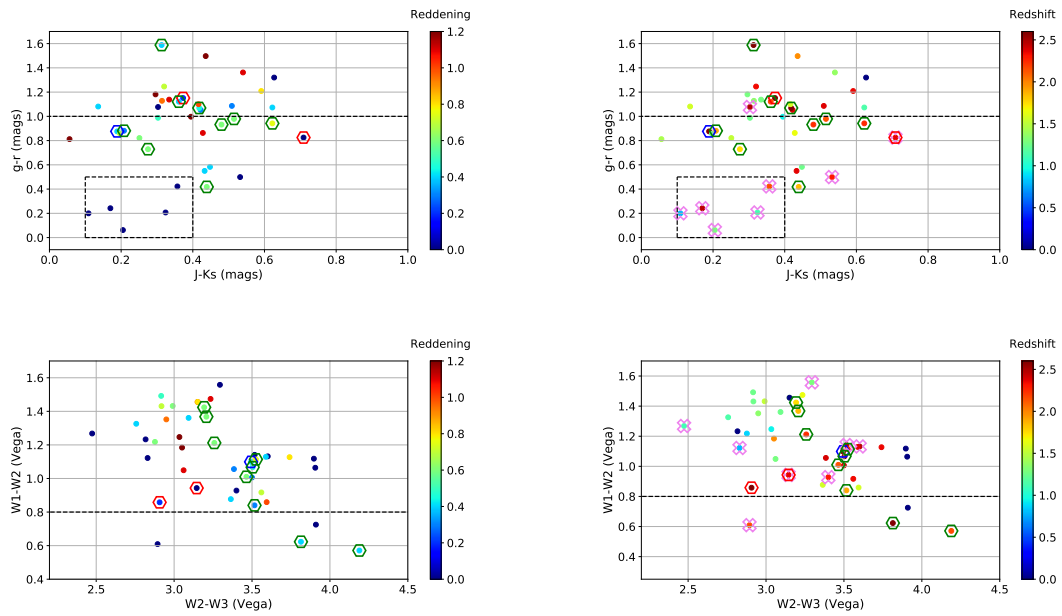


**Figure 3.8:** The full NOT and GTC sample colour coded depending on the reddening (left figures) and redshift (right figures). The red hexagones are BALs in the NOT sample, the blue hexagone is the normal bright BALs, and the green are the BALs in the GTC sample. The dashed selection box in the  $g-r$  vs  $J-Ks$  figures shows the location of the normal bright QSOs. The pink crosses show all the sources with zero reddening, in the redshift colour coded figures. The black dashed lines show the selection criteria.

### 3.5 DISCUSSION

The location of the SDSS spectroscopically confirmed quasars, the NOT and GTC targets are shown in optical colour space in the top panel of Figure 3.9. The plot shows the extent by which the purely optical selection methods are unsuccessful. While the normal bright QSOs are isolated in colour space, the observed red quasars are highly overlapping with the stellar track. This shows that optical surveys are missing a large population of red quasars and, thus are highly incomplete. It is notable that all the observed normal bright QSOs at the NOT are consistent with this separation, except for BrightJ2323+0057, which is overlapping with the stellar locus. This is the only QSO of the normal bright sample, that is a BAL and appears to be reddened ( $A_B=0.4$ ), while it has also the highest redshift ( $z=2.73$ ) of the sample. Moreover, it is seen that the low redshift quasars are concentrated in the bluest part of the ugr colour space, the quasars in the redshift range  $1 < z < 2$  start to approach the stellar track and the ones in the redshift range  $3 < z < 10$  are completely separated from the normal bright quasar locus and overlap with the stellar track. This confirms, as in Figure 1.3, that the u-g colour is highly ineffective in separating quasars at  $z > 2.5$  from stars.

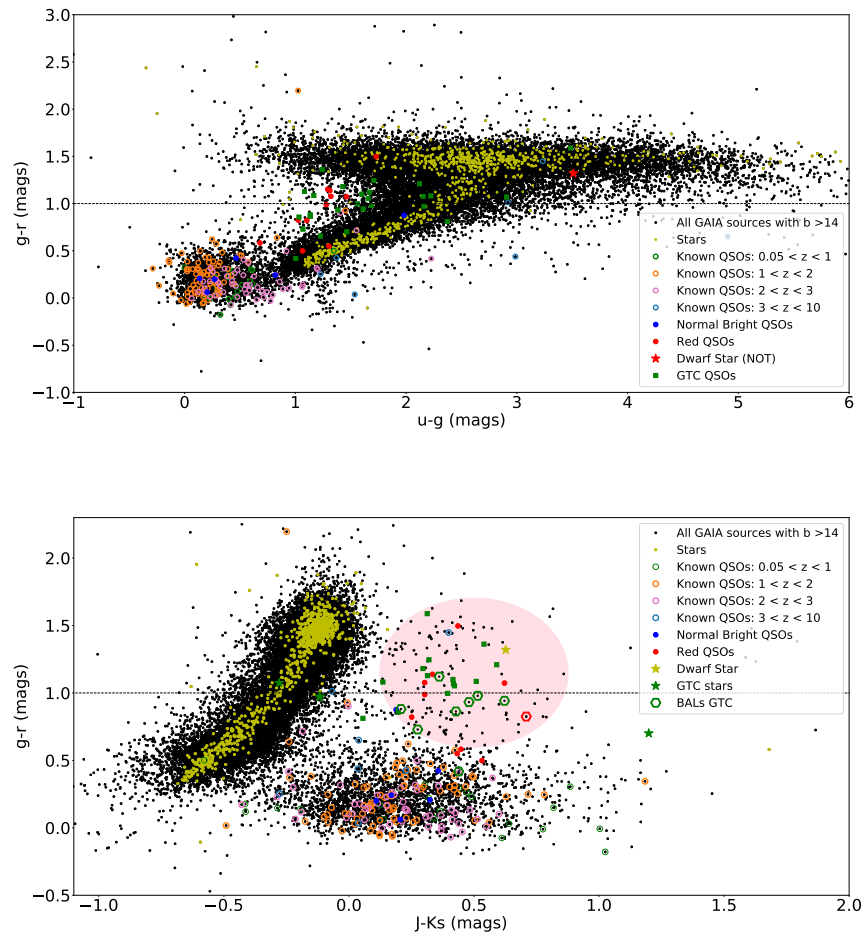


**Figure 3.9:** The quasar distribution shown in optical (*Top panel*) and optical/NIR (*Bottom panel:*) colour space. The same marker's convention as in Figure 3.5 is followed. The pink selection circle marks the area of the missing QSOs.

The bottom panel of Figure 3.9 shows more clearly the area, where the red quasars are located, which, as mentioned before, is isolated from both the stars and normal bright QSOs. The plot demonstrates how the UVX selection from SDSS is missing not only a large number of red quasars, but also a large number of BAL QSOs (seen in red (NOT) and green (GTC) hexagons).

While our selection criteria do not target any specific redshift range, it is seen in Figure 3.10 that 14 of the red QSOs are at  $z > 2.2$ . At  $z=2.2$  is the limit above which quasars lose their UV excess and are missed by UVX selection methods as shown in 1.2. Our selection criteria successfully detect reddened quasars above this redshift limit.

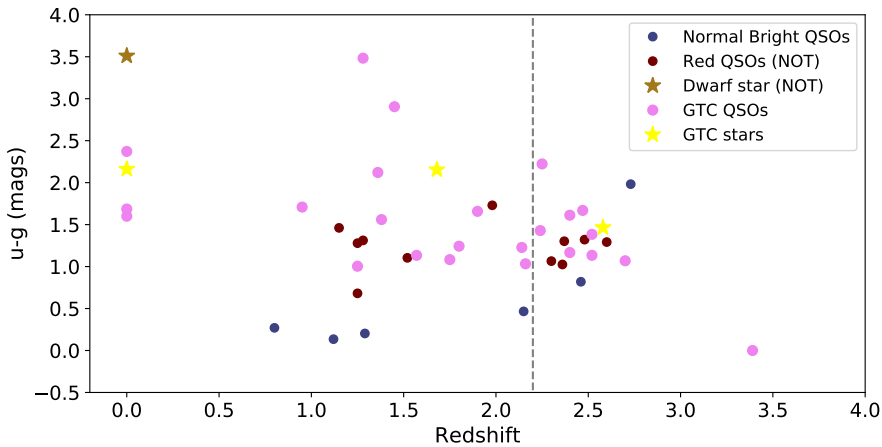


**Figure 3.10:** Optical u-g colour against the redshift of the NOT and GTC targets. The blue dots represent the normal bright QSOs, the red dots are the red QSOs observed with the NOT and the violet dots are the red QSOs observed with the GTC. The yellow stars show the M-dwarfs in the two samples. The grey dashed line shows the  $z=2.2$  limit above which the UVX method fails to detect red QSOs.

As proven above, optical colour selection criteria alone are highly inefficient in constructing a complete sample with low contamination. Thus, a better sample is acquired if optical and mid-infrared criteria are combined. Even though, mid-infrared selection has been found successful to find quasar candidates, this criterion is incapable of separating quasars from AGNs. To improve the quasar selection and reduce the bias as much as possible, optical, mid-infrared and proper motion criteria are combined. This combination reduces the contamination from stars to only 1.6 %, and this is mainly because of loosening of the criteria. Completeness cannot be claimed for such a small sample (39 targets, NOT+GTC), but it is already demonstrated that combining selection methods, reveals new populations of red quasars.

# 4 CONCLUSIONS

A sample of 12 candidate red quasars has been selected with a combination of optical, mid-infrared and proper motion criteria, for observation at the Nordic Optical Telescope (NOT). An additional sample of 6 normal bright quasars and 21 red quasars are used in this thesis. The purpose was to evaluate the effectiveness of this selection method, and to compare it to other existing selection techniques. The majority of quasars have previously been selected, based on their optical colours, and this method has extensively been used by large surveys like SDSS. Although, SDSS has identified a large number of QSOs, it appears to be very incomplete, since red quasars are not selected through optical colours, and as a result, are highly underrepresented.

To overcome this bias, the optical, mid-infrared and proper motion criteria were combined to identify 29 red quasars (NOT and GTC samples). From the total number of candidate red quasars in the NOT and GTC samples (33), only 4 were found to be stars. The quasars are illustrated in optical, near and mid-infrared colour space, and it is seen that red quasars are located in a separate locus than that of normal quasars and stars in near and mid-infrared colour space, but not in the optical.

After spectroscopic analysis of the 12 candidate red quasars that were observed at the NOT, 11 are classified as red quasars and one as M-dwarf star. Their redshift is calculated by identifying prominent emission lines in their spectra and the amount of reddening is determined by visual inspection of the spectra. The NOT sample contains only one star, which emerged due to the loosening of the selection criteria. This shows that, the chosen selection criteria are very important in avoiding stellar contamination, which is a common objective in every quasar survey. The sample, although small, is a good representation of the missing population of red quasars. Moreover, the red quasars are found in a field (Stripe 82) that has extensively been investigated by many surveys for QSOs. Even though they have been missed by other surveys, I present 11 new red quasars, proving the success of our selection

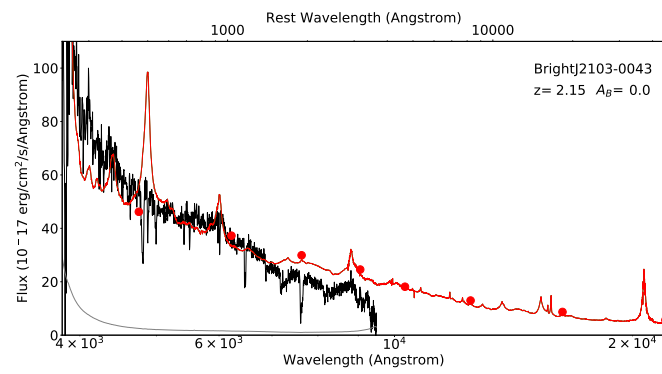
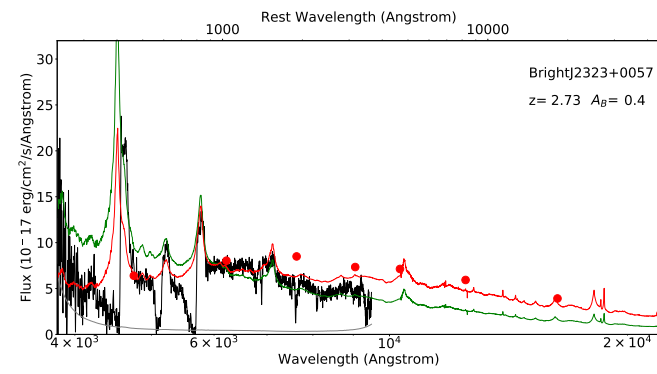
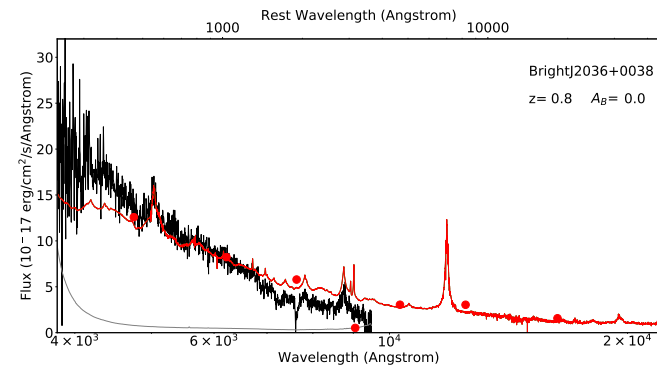
criteria, and the importance of exploring new selection techniques.

# Appendices

# A NORMAL BRIGHT QSOs

A sample of 6 normal bright quasars, observed by different teams during the same observing run in August 2018, was also used for comparison reasons, mainly in the colour diagrams. The normal bright quasars are spectroscopically classified and analysed following the same procedure as for the sample of the red quasars. The calculated redshifts and amount of reddening are shown in Table 3.2. The spectra of the 6 normal bright quasars are shown in B.1.

Within the sample only one target is a BAL QSO (BrightJ2323+0057) and appears to have a small amount of reddening ( $A_B = 0.4$ ). The redshift of BrightJ2323+0057 is determined by CIV and is the normal bright QSO with the highest redshift ( $z=2.73$ ). The lines SiIV, CIII are also identified, while Ly- $\alpha$  appears to be mostly absorbed by the Ly- $\alpha$  forest, so what is seen is the blended NV line in emission. All the other targets show no reddening ( $A_B = 0$ ), and among the sample, quasar BrightJ2103-0043 was the most non-trivial to spectroscopically classify, due to its very faint lines. The redshift is calculated by the MgII emission line, while CIII, CIV and SiIV are seen in absorption.



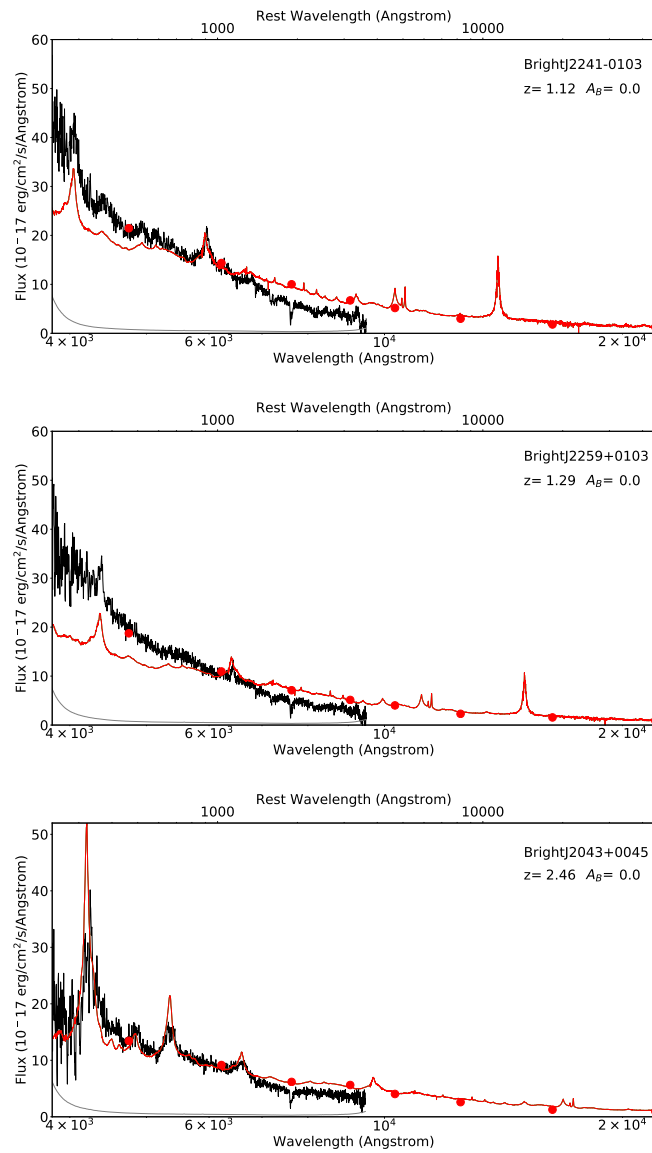
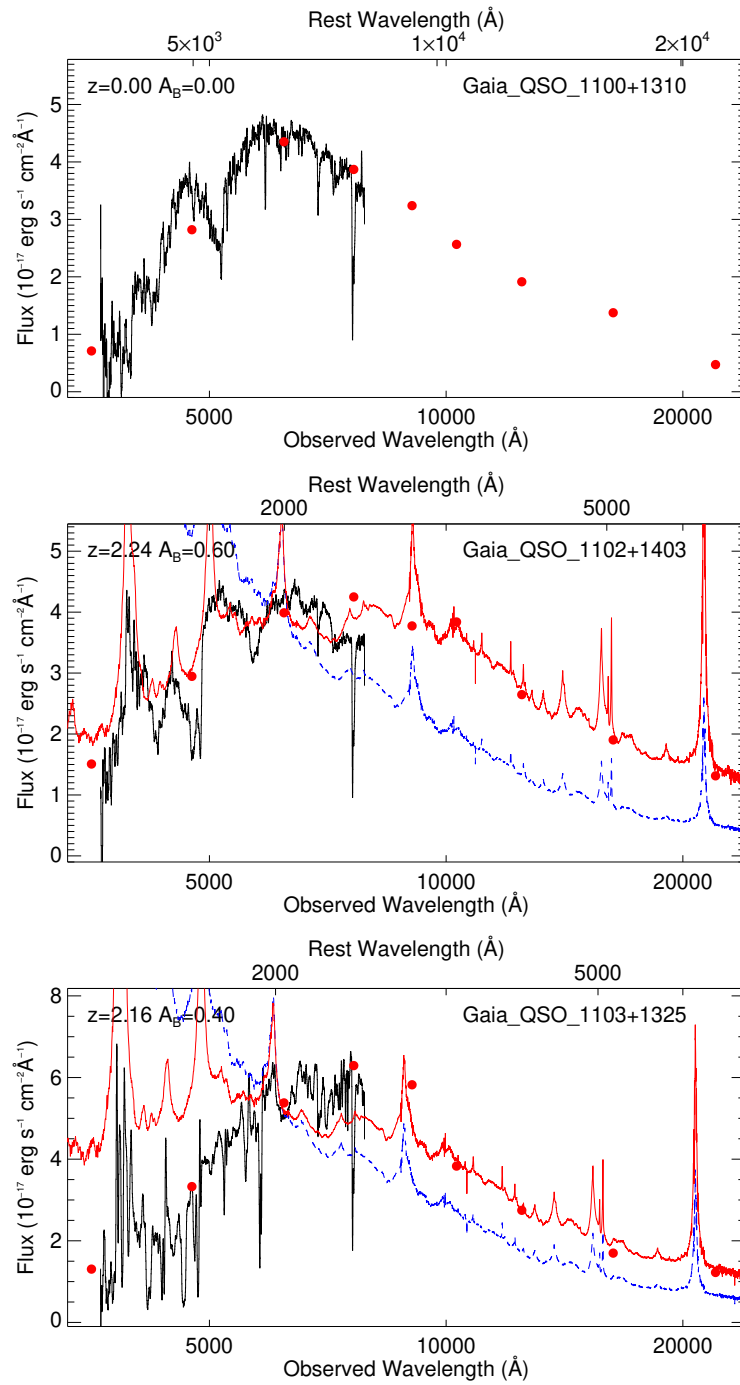
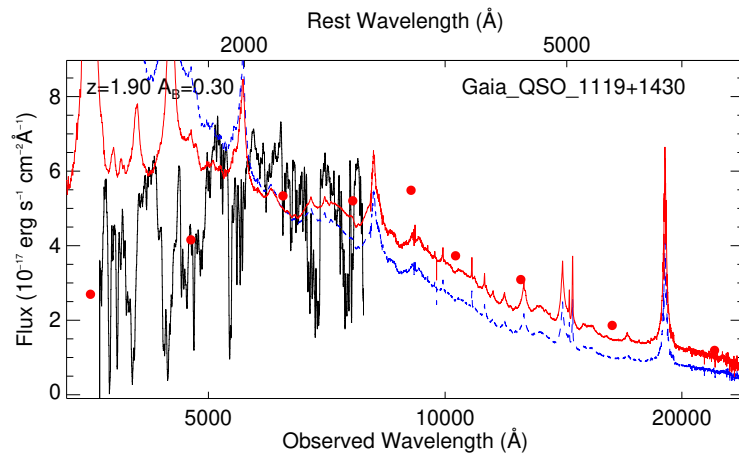
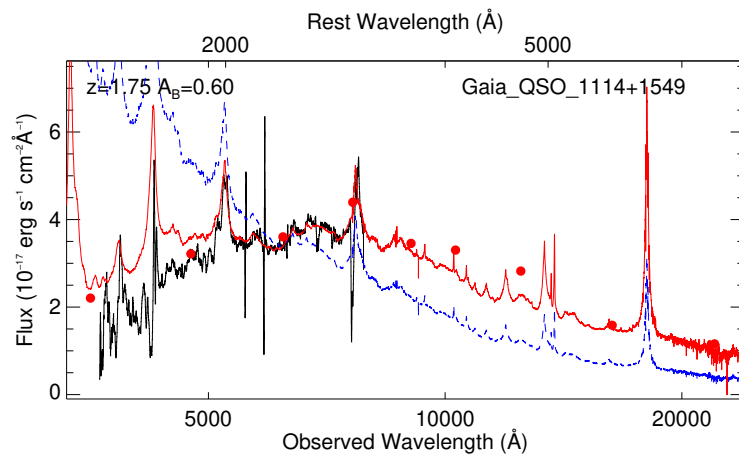
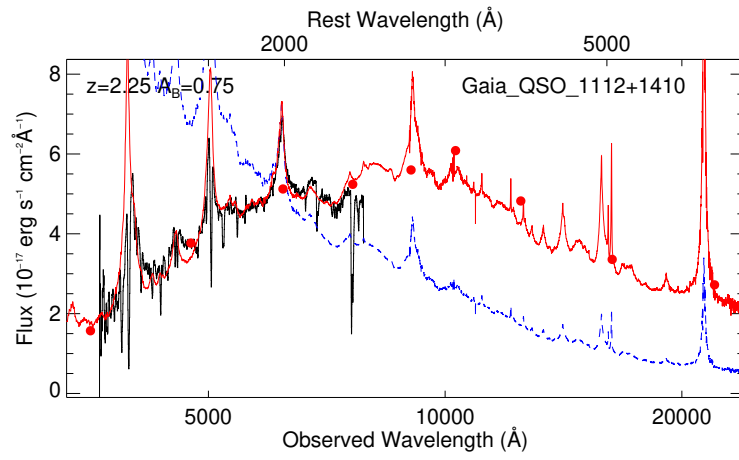


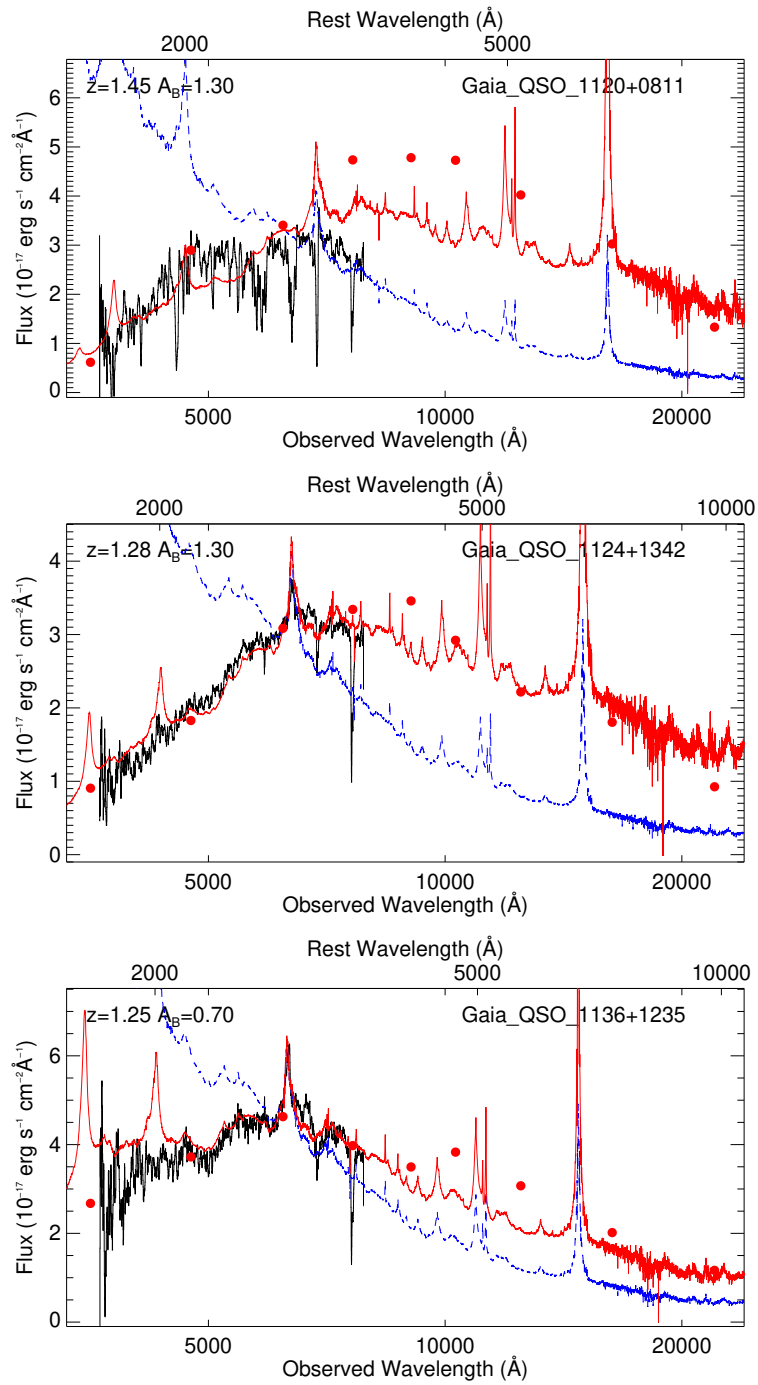
Figure A.1: The spectra of the normal bright quasars.

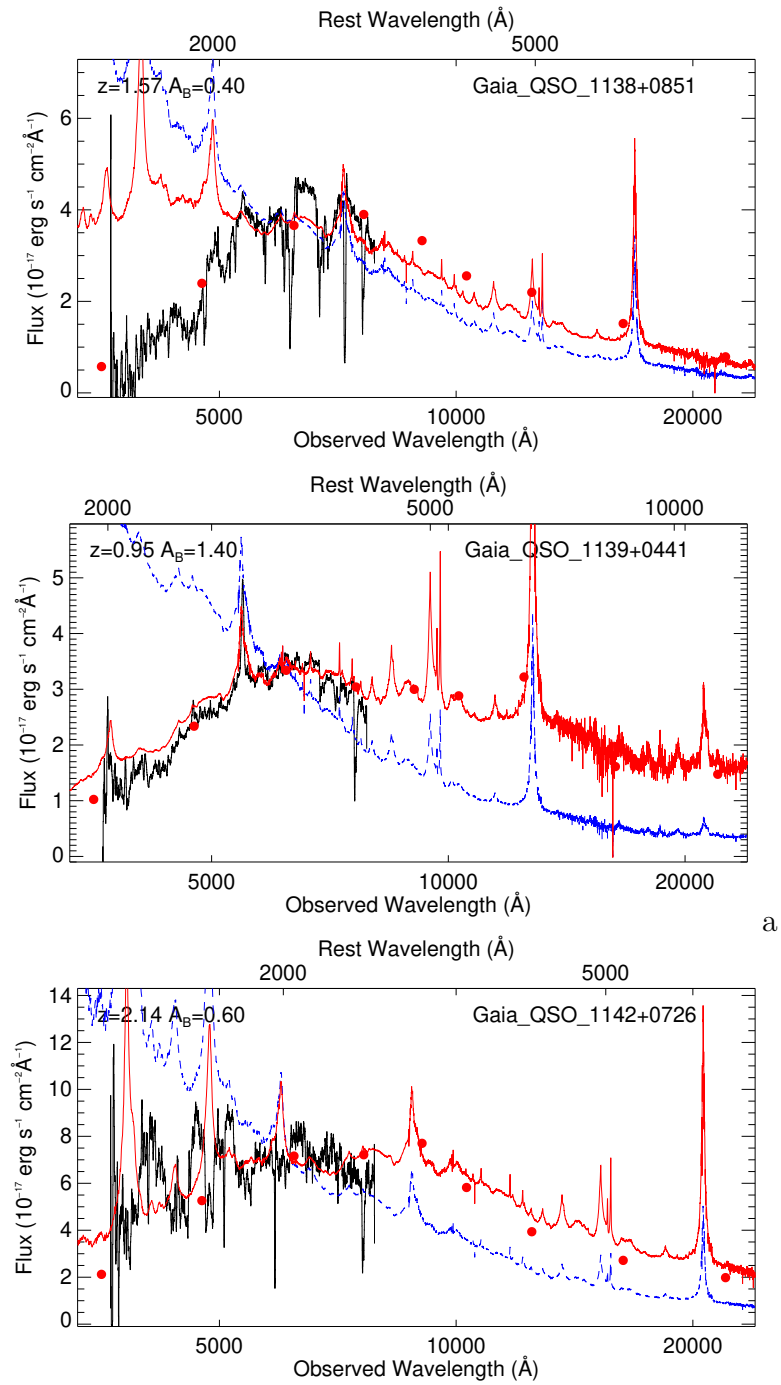
# B GTC SPECTRA

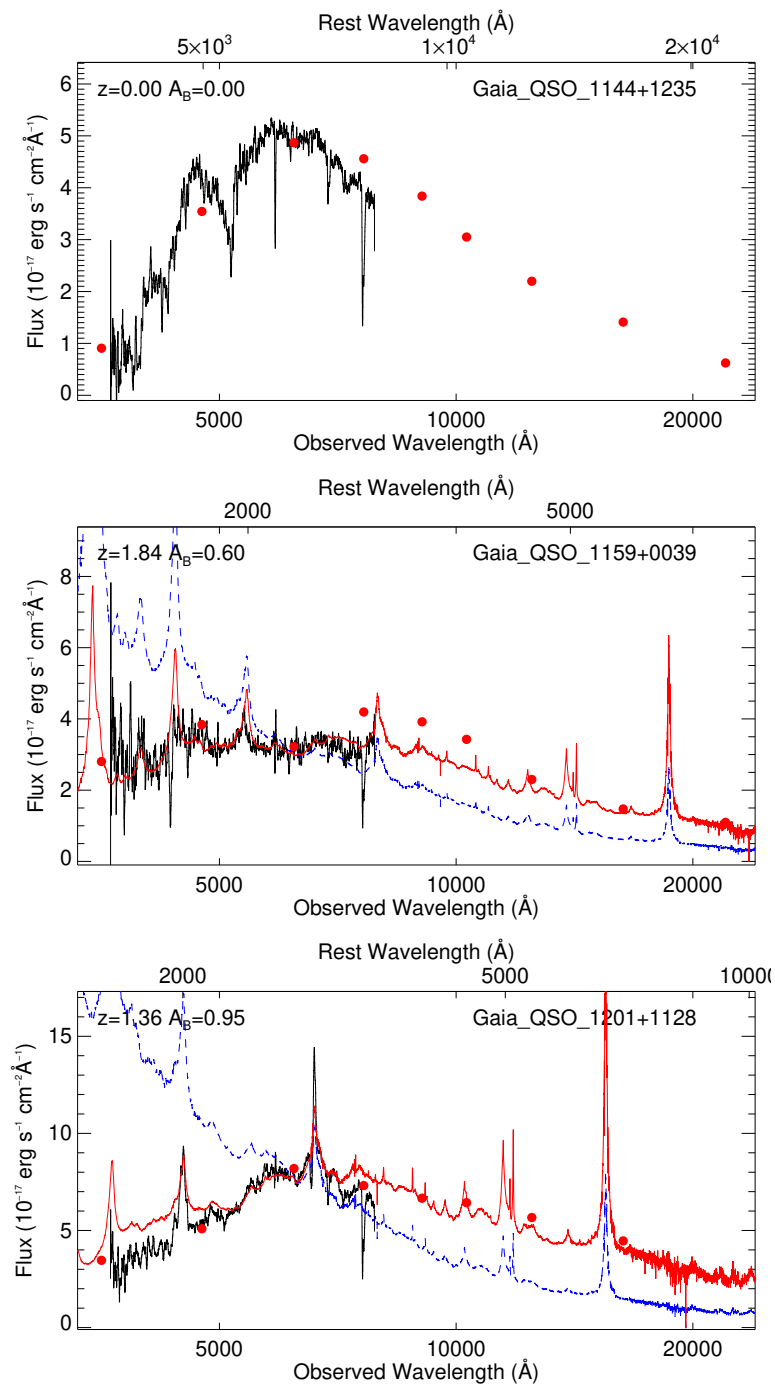
The targets were observed with the OSIRIS imager and spectrograph at the Gran Telescopio Canarias (GTC), with the aim of discovering quasars that are reddened specifically by Damped Lyman- $\alpha$  Absorbers (DLAs). First, they were selected based on astrometry from Gaia DR2, specifically targeting objects that have a Galactic latitude ( $b > 60\text{deg}$ ), and with zero proper-motion (within  $2\sigma$ ). Then, the near/mid-infrared criteria (UKIDSS and WISE) were imposed to limit the stellar contamination. Finally, two optical (SDSS) colour criteria were imposed, to target dust-reddened QSOs (Geier et al., 2019). As presented in Geier et al. (2019), Gaia\_QSO\_1218+0832 is a  $z=2.60$  QSO reddened by an intervening DLA at  $z=2.226$ . The sample contains 21 quasars, of which nine are BALs, and three contaminating stars. Most of the quasars have intermediate to high reddening and the redshift range is  $0.87 < z < 3.67$ . The sample is used in this work for completeness.

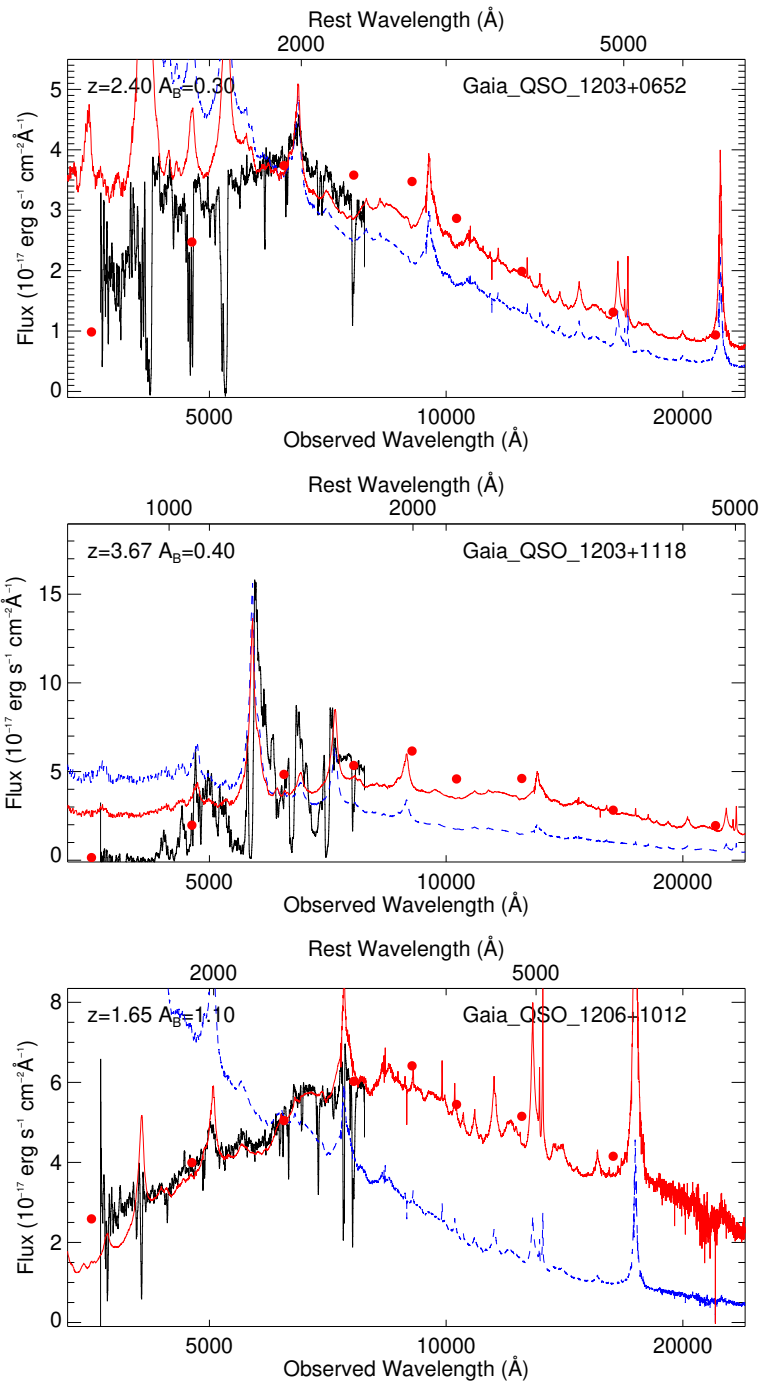


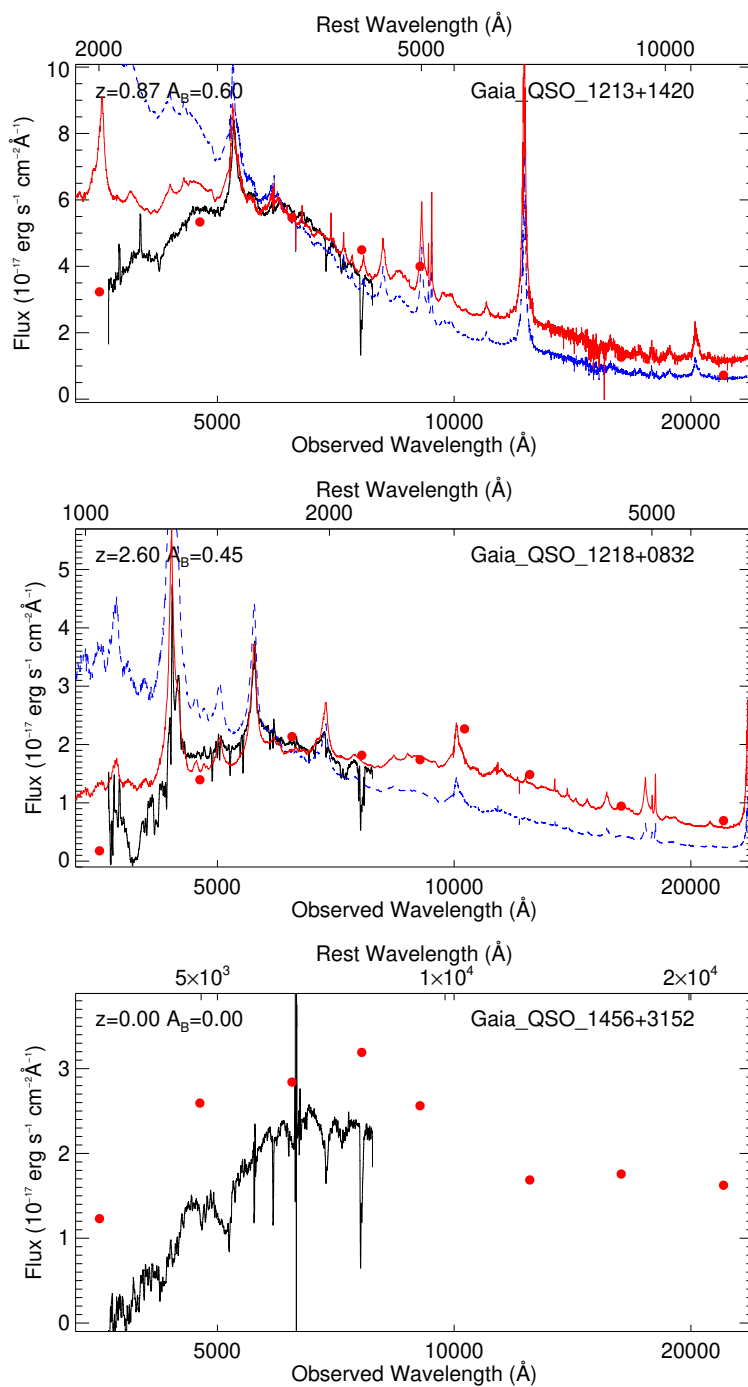












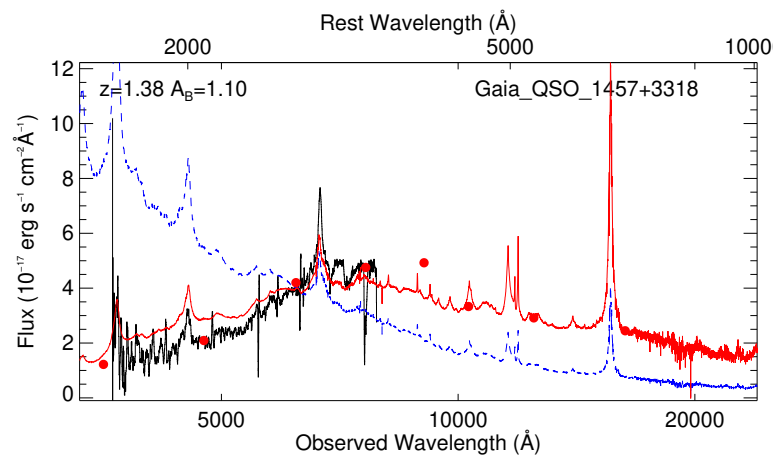


**Figure B.1:** The spectra of the targets observed with the GTC.

# BIBLIOGRAPHY

- N. Arav, G. Liu, X. Xu, J. Stidham, C. Benn, and C. Chamberlain. Evidence that 50% of BALQSO Outflows Are Situated at Least 100 pc from the Central Source. , 857:60, April 2018. doi: 10.3847/1538-4357/aab494.
- I. Aretxaga. AGN Variability: from Seyfert Nuclei to QSOs. In J. Franco, R. Terlevich, and A. Serrano, editors, *Revista Mexicana de Astronomía y Astrofísica Conference Series*, volume 6 of *Revista Mexicana de Astronomía y Astrofísica*, vol. 27, page 207, May 1997.
- E. Bañados, B. P. Venemans, C. Mazzucchelli, E. P. Farina, F. Walter, F. Wang, R. Decarli, D. Stern, X. Fan, F. B. Davies, J. F. Hennawi, R. A. Simcoe, M. L. Turner, H.-W. Rix, J. Yang, D. D. Kelson, G. C. Rudie, and J. M. Winters. An 800-million-solar-mass black hole in a significantly neutral Universe at a redshift of 7.5. , 553:473–476, January 2018. doi: 10.1038/nature25180.
- P. Barmby, A. Alonso-Herrero, J. L. Donley, E. Egami, G. G. Fazio, A. Georgakakis, J.-S. Huang, E. S. Laird, S. Miyazaki, K. Nandra, S. Q. Park, P. G. Pérez-González, G. H. Rieke, J. R. Rigby, and S. P. Willner. Mid-Infrared Properties of X-Ray Sources in the Extended Groth Strip. , 642:126–139, May 2006. doi: 10.1086/500823.
- R. H. Becker, R. L. White, and D. J. Helfand. The FIRST Survey: Faint Images of the Radio Sky at Twenty Centimeters. , 450:559, September 1995. doi: 10.1086/176166.
- B. J. Boyle, T. Shanks, S. M. Croom, R. J. Smith, L. Miller, N. Loaring, and C. Heymans. The 2dF QSO Redshift Survey - I. The optical luminosity function of quasi-stellar objects. , 317:1014–1022, October 2000. doi: 10.1046/j.1365-8711.2000.03730.x.

F. Civano, S. Marchesi, A. Comastri, M. C. Urry, M. Elvis, N. Cappelluti, S. Puccetti, M. Brusa, G. Zamorani, G. Hasinger, T. Aldcroft, D. M. Alexander, V. Allevato, H. Brunner, P. Capak, A. Finoguenov, F. Fiore, A. Fruscione, R. Gilli, K. Glotfelty, R. E. Griffiths, H. Hao, F. A. Harrison, K. Jahnke, J. Kartaltepe, A. Karim, S. M. LaMassa, G. Lanzuisi, T. Miyaji, P. Ranalli, M. Salvato, M. Sargent, N. J. Scoville, K. Schawinski, E. Schinnerer, J. Silverman, V. Smolcic, D. Stern, S. Toft, B. Trakhtenbrot, E. Treister, and C. Vignali. The Chandra Cosmos Legacy Survey: Overview and Point Source Catalog. , 819:62, Mar 2016. doi: 10.3847/0004-637X/819/1/62.

Daniel J. Eisenstein, David H. Weinberg, Eric Agol, Hiroaki Aihara, Carlos Allende Prieto, Scott F. Anderson, James A. Arns, Éric Aubourg, Stephen Bailey, Eduardo Balbinot, Robert Barkhouser, Timothy C. Beers, Andreas A. Berlind, Steven J. Bickerton, Dmitry Bizyaev, Michael R. Blanton, John J. Bochanski, Adam S. Bolton, Casey T. Bosman, Jo Bovy, W. N. Brandt, Ben Breslauer, Howard J. Brewington, J. Brinkmann, Peter J. Brown, Joel R. Brownstein, Dan Burger, Nicolas G. Busca, Heather Campbell, Phillip A. Cargile, William C. Carithers, Joleen K. Carlberg, Michael A. Carr, Liang Chang, Yanmei Chen, Cristina Chiappini, Johan Comparat, Natalia Connolly, Marina Cortes, Rupert A. C. Croft, Katia Cunha, Luiz N. da Costa, James R. A. Davenport, Kyle Dawson, Nathan De Lee, Gustavo F. Porto de Mello, Fernando de Simoni, Janice Dean, Saurav Dhital, Anne Ealet, Garrett L. Ebelke, Edward M. Edmondson, Jacob M. Eiting, Stephanie Escoffier, Massimiliano Esposito, Michael L. Evans, Xiaohui Fan, Bruno Femenía Castellá, Leticia Dutra Ferreira, Greg Fitzgerald, Scott W. Fleming, Andreu Font-Ribera, Eric B. Ford, Peter M. Frinchaboy, Ana Elia García Pérez, B. Scott Gaudi, Jian Ge, Luan Ghezzi, Bruce A. Gillespie, G. Gilmore, Léo Girardi, J. Richard Gott, Andrew Gould, Eva K. Grebel, James E. Gunn, Jean-Christophe Hamilton, Paul Harding, David W. Harris, Suzanne L. Hawley, Frederick R. Hearty, Joseph F. Hennawi, Jonay I. González Hernández, Shirley Ho, David W. Hogg, Jon A. Holtzman, Klaus Honscheid, Naohisa Inada, Inese I. Ivans, Linhua Jiang, Peng Jiang, Jennifer A. Johnson, Cathy Jordan, Wendell P. Jordan, Guinevere Kauffmann, Eyal Kazin, David Kirkby, Mark A. Klaene, G. R. Knapp, Jean-Paul Kneib, C. S. Kochanek, Lars Koesterke, Juna A. Kollmeier, Richard G. Kron, Hubert Lampeitl, Dustin Lang, James E. Lawler, Jean-Marc Le Goff, Brian L. Lee, Young Sun Lee, Jarron M. Leisenring, Yen-Ting Lin, Jian Liu, Daniel C. Long, Craig P. Loomis, Sara Lucatello, Britt Lundgren, Robert H. Lupton, Bo Ma, Zhibo Ma, Nicholas MacDonald, Claude Mack, Suvrath Mahadevan, Marcio A. G. Maia, Steven R. Majewski, Martin Makler, Elena Malanushenko, Viktor Malanushenko, Rachel Mandelbaum, Claudia Maraston, Daniel Margala, Paul Maseman, Karen L. Masters, Cameron K. McBride, Patrick Mc-

- Donald, Ian D. McGreer, Richard G. McMahon, Olga Mena Requejo, Brice Ménard, Jordi Miralda-Escudé, Heather L. Morrison, Fergal Mullally, Demitri Muna, Hitoshi Murayama, Adam D. Myers, Tracy Naugle, Angelo Fausti Neto, Duy Cuong Nguyen, Robert C. Nichol, David L. Nidever, Robert W. O’Connell, Ricardo L. C. Ogando, Matthew D. Olmstead, Daniel J. Oravetz, Nikhil Padmanabhan, Martin Paegert, Nathalie Palanque-Delabrouille, Kaike Pan, Parul Pandey, John K. Parejko, Isabelle Pâris, Paulo Pellegrini, Joshua Pepper, Will J. Percival, Patrick Petitjean, Robert Pfaffenberger, Janine Pforr, Stefanie Phleps, Christophe Pichon, Matthew M. Pieri, Francisco Prada, Adrian M. Price-Whelan, M. Jordan Raddick, Beatriz H. F. Ramos, I. Neill Reid, Celine Reyle, James Rich, Gordon T. Richards, George H. Rieke, Marcia J. Rieke, Hans-Walter Rix, Annie C. Robin, Helio J. Rocha-Pinto, Constance M. Rockosi, Natalie A. Roe, Emmanuel Rollinde, Ashley J. Ross, Nicholas P. Ross, Bruno Rossetto, Ariel G. Sánchez, Basilio Santiago, Conor Sayres, Ricardo Schivon, David J. Schlegel, Katharine J. Schlesinger, Sarah J. Schmidt, Donald P. Schneider, Kris Sellgren, Alaina Shelden, Erin Sheldon, Matthew Shetrone, Yiping Shu, John D. Silverman, Jennifer Simmerer, Audrey E. Simmons, Thirupathi Sivarani, M. F. Skrutskie, Anže Slosar, Stephen Smeed, Verne V. Smith, Stephanie A. Snedden, Keivan G. Stassun, Oliver Steele, Matthias Steinmetz, Mark H. Stockett, Todd Stollberg, Michael A. Strauss, Alexander S. Szalay, Masayuki Tanaka, Aniruddha R. Thakar, Daniel Thomas, Jeremy L. Tinker, Benjamin M. Tofflemire, Rita Tojeiro, Christy A. Tremonti, Mariana Vargas Magaña, Licia Verde, Nicole P. Vogt, David A. Wake, Xiaoke Wan, Ji Wang, Benjamin A. Weaver, Martin White, Simon D. M. White, John C. Wilson, John P. Wisniewski, W. Michael Wood-Vasey, Brian Yanny, Naoki Yasuda, Christophe Yèche, Donald G. York, Erick Young, Gail Zasowski, Idit Zehavi, and Bo Zhao. SDSS-III: Massive Spectroscopic Surveys of the Distant Universe, the Milky Way, and Extra-Solar Planetary Systems. , 142(3):72, Sep 2011. doi: 10.1088/0004-6256/142/3/72.
- M. Elvis. The Chandra COSMOS Survey. In *American Astronomical Society Meeting Abstracts #214*, volume 214 of *American Astronomical Society Meeting Abstracts*, page 708, May 2009.
- Stefan Geier, Kasper Elm Heintz, Johan Fynbo, Cédric Ledoux, Lise Christensen, Pall Jakobsson, Jens-Kristian Krogager, Bo Milvang-Jensen, Palle Møller, and Pasquier Noterdaeme. Gaia-assisted selection of a quasar reddened by dust in an extremely-strong Damped Lyman- $\alpha$  Absorber at  $z=2.226$ . *arXiv e-prints*, art. arXiv:1904.01686, Apr 2019.
- G. Gilmore, S. Randich, M. Asplund, J. Binney, P. Bonifacio, J. Drew, S. Feltzing,

- A. Ferguson, R. Jeffries, G. Micela, and et al. The Gaia-ESO Public Spectroscopic Survey. *The Messenger*, 147:25–31, March 2012.
- A. Grazian, S. Cristiani, V. D’Odorico, A. Omizzolo, and A. Pizzella. The Asiago-ESO/RASS QSO Survey. I. The Catalog and the Local QSO Luminosity Function. , 119:2540–2555, June 2000. doi: 10.1086/301398.
- J. L. Greenstein and M. Schmidt. The Quasi-Stellar Radio Sources 3C 48 and 3C 273. , 140:1, July 1964. doi: 10.1086/147889.
- Sufen Guo, Zhaoxiang Qi, Shilong Liao, Zihuang Cao, Mario G. Lattanzi, Beatrice Bucciarelli, Zhenghong Tang, and Qing-Zeng Yan. Identifying quasars with astrometric and mid-infrared methods from APOP and ALLWISE. , 618:A144, Oct 2018. doi: 10.1051/0004-6361/201833135.
- G. Hasinger, N. Cappelluti, H. Brunner, M. Brusa, A. Comastri, M. Elvis, A. Finoguenov, F. Fiore, A. Franceschini, R. Gilli, R. E. Griffiths, I. Lehmann, V. Mainieri, G. Matt, I. Matute, T. Miyaji, S. Molendi, S. Paltani, D. B. Sanders, N. Scoville, L. Tresse, C. M. Urry, P. Vettolani, and G. Zamorani. The XMM-Newton Wide-Field Survey in the COSMOS Field. I. Survey Description. , 172: 29–37, September 2007. doi: 10.1086/516576.
- M. R. S. Hawkins. Dark matter from quasar microlensing. , 278:787–807, February 1996. doi: 10.1093/mnras/278.3.787.
- K. E. Heintz, J. P. U. Fynbo, and E. Høg. A study of purely astrometric selection of extragalactic point sources with Gaia. , 578:A91, June 2015. doi: 10.1051/0004-6361/201526038.
- P. C. Hewett and C. B. Foltz. The Frequency and Radio Properties of Broad Absorption Line Quasars. , 125:1784–1794, April 2003. doi: 10.1086/368392.
- Ž. Ivezić, K. Menou, G. R. Knapp, M. A. Strauss, R. H. Lupton, D. E. Vanden Berk, G. T. Richards, C. Tremonti, M. A. Weinstein, S. Anderson, N. A. Bahcall, R. H. Becker, M. Bernardi, M. Blanton, D. Eisenstein, X. Fan, D. Finkbeiner, K. Finlator, J. Frieman, J. E. Gunn, P. B. Hall, R. S. J. Kim, A. Kinkhabwala, V. K. Narayanan, C. M. Rockosi, D. Schlegel, D. P. Schneider, I. Strateva, M. SubbaRao, A. R. Thakar, W. Voges, R. L. White, B. Yanny, J. Brinkmann, M. Doi, M. Fukugita, G. S. Hennessy, J. A. Munn, R. C. Nichol, and D. G. York. Optical and Radio Properties of Extragalactic Sources Observed by the FIRST Survey and the Sloan Digital Sky Survey. , 124:2364–2400, November 2002. doi: 10.1086/344069.

- F. Jansen, D. Lumb, B. Altieri, J. Clavel, M. Ehle, C. Erd, C. Gabriel, M. Guainazzi, P. Gondoin, R. Much, R. Munoz, M. Santos, N. Schartel, D. Textier, and G. Vacanti. XMM-Newton observatory. I. The spacecraft and operations. , 365:L1–L6, January 2001. doi: 10.1051/0004-6361:20000036.
- A.K. Kembhavi and J.V. Narlikar. *Quasars and Active Galactic Nuclei: An Introduction*. Cambridge University Press, 1999. ISBN 9780521479899. URL <https://books.google.dk/books?id=v07KDjwzUK4C>.
- A. King. The Connection between ULX’s and Massive BHs, BH Formation. In *KITP Conference: Globular Clusters: Formation, Evolution and the Role of Compact Objects*, page 23, January 2003.
- R. G. Kron and L.-T. G. Chiu. Stars with zero proper motion and the number of faint QSOs. , 93:397–404, August 1981. doi: 10.1086/130845.
- M. Lacy, L. J. Storrie-Lombardi, A. Sajina, P. N. Appleton, L. Armus, S. C. Chapman, P. I. Choi, D. Fadda, F. Fang, D. T. Frayer, I. Heinrichsen, G. Helou, M. Im, F. R. Marleau, F. Masci, D. L. Shupe, B. T. Soifer, J. Surace, H. I. Teplitz, G. Wilson, and L. Yan. Obscured and Unobscured Active Galactic Nuclei in the Spitzer Space Telescope First Look Survey. , 154:166–169, September 2004. doi: 10.1086/422816.
- A. Lawrence, S. J. Warren, O. Almaini, A. C. Edge, N. C. Hambly, R. F. Jameson, P. Lucas, M. Casali, A. Adamson, S. Dye, J. P. Emerson, S. Foucaud, P. Hewett, P. Hirst, S. T. Hodgkin, M. J. Irwin, N. Lodieu, R. G. McMahon, C. Simpson, I. Smail, D. Mortlock, and M. Folger. The UKIRT Infrared Deep Sky Survey (UKIDSS). , 379:1599–1617, August 2007. doi: 10.1111/j.1365-2966.2007.12040.x.
- N. Maddox, P. C. Hewett, S. J. Warren, and S. M. Croom. Luminous K-band selected quasars from UKIDSS. , 386:1605–1624, May 2008. doi: 10.1111/j.1365-2966.2008.13138.x.
- N. Maddox, P. C. Hewett, C. Péroux, D. B. Nestor, and L. Wisotzki. The large area KX quasar catalogue - I. Analysis of the photometric redshift selection and the complete quasar catalogue. , 424:2876–2895, August 2012. doi: 10.1111/j.1365-2966.2012.21427.x.
- S. Mateos, A. Alonso-Herrero, F. J. Carrera, A. Blain, M. G. Watson, X. Barcons, V. Braitto, P. Severgnini, J. L. Donley, and D. Stern. Using the Bright Ultrahard XMM-Newton survey to define an IR selection of luminous AGN based on WISE colours. , 426(4):3271–3281, Nov 2012. doi: 10.1111/j.1365-2966.2012.21843.x.

- N. Murray, J. Chiang, S. A. Grossman, and G. M. Voit. Accretion Disk Winds from Active Galactic Nuclei. , 451:498, October 1995. doi: 10.1086/176238.
- P. S. Osmer and M. G. Smith. The emission-line spectra of nine newly discovered, optically selected quasars with redshift 2.5 to 3.1. , 210:267–276, November 1976. doi: 10.1086/154827.
- Y. C. Pei. Interstellar dust from the Milky Way to the Magellanic Clouds. , 395:130–139, August 1992. doi: 10.1086/171637.
- M. A. C. Perryman, L. Lindegren, J. Kovalevsky, E. Hog, U. Bastian, P. L. Bernacca, M. Creze, F. Donati, M. Grenon, M. Grewing, F. van Leeuwen, H. van der Marel, F. Mignard, C. A. Murray, R. S. Le Poole, H. Schrijver, C. Turon, F. Arenou, M. Froeschle, and C. S. Petersen. The Hipparcos Catalogue. , 500:501–504, Jul 1997.
- B. M. Peterson. *An Introduction to Active Galactic Nuclei*. February 1997.
- Planck Collaboration, P. A. R. Ade, N. Aghanim, M. Arnaud, M. Ashdown, J. Aumont, C. Baccigalupi, A. J. Banday, R. B. Barreiro, J. G. Bartlett, and et al. Planck 2015 results. XIII. Cosmological parameters. , 594:A13, September 2016. doi: 10.1051/0004-6361/201525830.
- M. J. Rees. Comments on the physics of active galactic nuclei. In W. Brinkmann and J. Truemper, editors, *X-ray and UV Emission from Active Galactic Nuclei*, October 1984.
- Gordon T. Richards, Michael A. Strauss, Xiaohui Fan, Patrick B. Hall, Sebastian Jester, Donald P. Schneider, Daniel E. Vanden Berk, Chris Stoughton, Scott F. Anderson, Robert J. Brunner, Jim Gray, James E. Gunn, Željko Ivezić, Margaret K. Kirkland , G. R. Knapp, Jon Loveday, Avery Meiksin, Adrian Pope, Alexander S. Szalay, Anirudda R. Thakar, Brian Yanny, Donald G. York, J. C. Barentine, Howard J. Brewington, J. Brinkmann, Masataka Fukugita, Michael Harvanek, Stephen M. Kent, S. J. Kleinman, Jurek Krzesiński, Daniel C. Long, Robert H. Lupton, Thomas Nash, Jr. Neilsen, Eric H., Atsuko Nitta, David J. Schlegel, and Stephanie A. Snedden. The Sloan Digital Sky Survey Quasar Survey: Quasar Luminosity Function from Data Release 3. , 131:2766–2787, Jun 2006. doi: 10.1086/503559.
- E. E. Salpeter. Accretion of Interstellar Matter by Massive Objects. , 140:796–800, August 1964. doi: 10.1086/147973.
- A. Sandage. The Existence of a Major New Constituent of the Universe: the Quasistellar Galaxies. , 141:1560, May 1965. doi: 10.1086/148245.

- D. J. Schlegel, D. P. Finkbeiner, and M. Davis. Maps of Dust Infrared Emission for Use in Estimation of Reddening and Cosmic Microwave Background Radiation Foregrounds. , 500:525–553, June 1998. doi: 10.1086/305772.
- Kasper B. Schmidt, Philip J. Marshall, Hans-Walter Rix, Sebastian Jester, Joseph F. Hennawi, and Gregory Dobler. Selecting Quasars by Their Intrinsic Variability. , 714:1194–1208, May 2010. doi: 10.1088/0004-637X/714/2/1194.
- M. Schmidt. 3C 273 : A Star-Like Object with Large Red-Shift. , 197:1040, March 1963. doi: 10.1038/1971040a0.
- M. Schmidt and R. F. Green. Quasar evolution derived from the Palomar bright quasar survey and other complete quasar surveys. , 269:352–374, June 1983. doi: 10.1086/161048.
- J. Selsing, J. P. U. Fynbo, L. Christensen, and J.-K. Krogager. An X-Shooter composite of bright  $1 < z < 2$  quasars from UV to infrared. , 585:A87, January 2016. doi: 10.1051/0004-6361/201527096.
- P. A. Shaver, J. V. Wall, K. I. Kellermann, C. A. Jackson, and M. R. S. Hawkins. Decrease in the space density of quasars at high redshift. , 384:439–441, December 1996. doi: 10.1038/384439a0.
- M. F. Skrutskie, R. M. Cutri, R. Stiening, M. D. Weinberg, S. Schneider, J. M. Carpenter, C. Beichman, R. Capps, T. Chester, J. Elias, J. Huchra, J. Liebert, C. Lonsdale, D. G. Monet, S. Price, P. Seitzer, T. Jarrett, J. D. Kirkpatrick, J. E. Gizis, E. Howard, T. Evans, J. Fowler, L. Fullmer, R. Hurt, R. Light, E. L. Kopan, K. A. Marsh, H. L. McCallon, R. Tam, S. Van Dyk, and S. Wheelock. The Two Micron All Sky Survey (2MASS). , 131:1163–1183, February 2006. doi: 10.1086/498708.
- M. G. Smith. Emission-line galaxies and quasars in the Southern Hemisphere. I - Description and applications of an objective-prism survey. , 202:591–595, December 1975. doi: 10.1086/154011.
- D. Stern, R. J. Assef, D. J. Benford, A. Blain, R. Cutri, A. Dey, P. Eisenhardt, R. L. Griffith, T. H. Jarrett, S. Lake, F. Masci, S. Petty, S. A. Stanford, C.-W. Tsai, E. L. Wright, L. Yan, F. Harrison, and K. Madsen. Mid-infrared Selection of Active Galactic Nuclei with the Wide-Field Infrared Survey Explorer. I. Characterizing WISE-selected Active Galactic Nuclei in COSMOS. , 753:30, July 2012. doi: 10.1088/0004-637X/753/1/30.
- J. Terrell. Quasi-Stellar Diameters and Intensity Fluctuations. *Science*, 145:918–919, August 1964. doi: 10.1126/science.145.3635.918.

- P. G. van Dokkum. Cosmic-Ray Rejection by Laplacian Edge Detection. , 113: 1420–1427, November 2001. doi: 10.1086/323894.
- S. J. Warren, P. C. Hewett, M. J. Irwin, R. G. McMahon, and M. T. Bridgeland. First observation of a quasar with a redshift of 4. , 325:131–133, January 1987. doi: 10.1038/325131a0.
- S. J. Warren, P. C. Hewett, and C. B. Foltz. The KX method for producing K-band flux-limited samples of quasars. , 312:827–832, March 2000. doi: 10.1046/j.1365-8711.2000.03206.x.
- S. J. Warren, N. C. Hambly, S. Dye, O. Almaini, N. J. G. Cross, A. C. Edge, S. Foucaud, P. C. Hewett, S. T. Hodgkin, M. J. Irwin, R. F. Jameson, A. Lawrence, P. W. Lucas, A. J. Adamson, R. M. Bandyopadhyay, J. Bryant, R. S. Collins, C. J. Davis, J. S. Dunlop, J. P. Emerson, D. W. Evans, E. A. Gonzales-Solares, P. Hirst, M. J. Jarvis, T. R. Kendall, T. H. Kerr, S. K. Leggett, J. R. Lewis, R. G. Mann, R. J. McLure, R. G. McMahon, D. J. Mortlock, M. G. Rawlings, M. A. Read, M. Riello, C. Simpson, D. J. B. Smith, E. T. W. Sutorius, T. A. Targett, and W. P. Varricatt. The United Kingdom Infrared Telescope Infrared Deep Sky Survey First Data Release. , 375(1):213–226, Feb 2007. doi: 10.1111/j.1365-2966.2006.11284.x.
- M. C. Weisskopf, B. Brinkman, C. Canizares, G. Garmire, S. Murray, and L. P. Van Speybroeck. An Overview of the Performance and Scientific Results from the Chandra X-Ray Observatory. *Publications of the Astronomical Society of the Pacific*, 114:1–24, Jan 2002. doi: 10.1086/338108.
- R. J. Weymann, R. F. Carswell, and M. G. Smith. Absorption lines in the spectra of quasistellar objects. , 19:41–76, 1981. doi: 10.1146/annurev.aa.19.090181.000353.
- E. L. Wright, P. R. M. Eisenhardt, A. K. Mainzer, M. E. Ressler, R. M. Cutri, T. Jarrett, J. D. Kirkpatrick, D. Padgett, R. S. McMillan, M. Skrutskie, S. A. Stanford, M. Cohen, R. G. Walker, J. C. Mather, D. Leisawitz, T. N. Gautier, III, I. McLean, D. Benford, C. J. Lonsdale, A. Blain, B. Mendez, W. R. Irace, V. Duval, F. Liu, D. Royer, I. Heinrichsen, J. Howard, M. Shannon, M. Kendall, A. L. Walsh, M. Larsen, J. G. Cardon, S. Schick, M. Schwalm, M. Abid, B. Fabinsky, L. Naes, and C.-W. Tsai. The Wide-field Infrared Survey Explorer (WISE): Mission Description and Initial On-orbit Performance. , 140: 1868–1881, December 2010. doi: 10.1088/0004-6256/140/6/1868.
- X. Xu, N. Arav, T. Miller, and C. Benn. VLT/X-Shooter Survey of BAL Quasars: Large Distance Scale and AGN Feedback. *arXiv e-prints*, May 2018.

- D. G. York, J. Adelman, J. E. Anderson, Jr., S. F. Anderson, J. Annis, N. A. Bahcall, J. A. Bakken, R. Barkhouser, S. Bastian, E. Berman, W. N. Boroski, S. Bracker, C. Briegel, J. W. Briggs, J. Brinkmann, R. Brunner, S. Burles, L. Carey, M. A. Carr, F. J. Castander, B. Chen, P. L. Colestock, A. J. Connolly, J. H. Crocker, I. Csabai, P. C. Czarapata, J. E. Davis, M. Doi, T. Dombeck, D. Eisenstein, N. Ellman, B. R. Elms, M. L. Evans, X. Fan, G. R. Federwitz, L. Fiscelli, S. Friedman, J. A. Frieman, M. Fukugita, B. Gillespie, J. E. Gunn, V. K. Gurbani, E. de Haas, M. Haldeman, F. H. Harris, J. Hayes, T. M. Heckman, G. S. Hennessy, R. B. Hindsley, S. Holm, D. J. Holmgren, C.-h. Huang, C. Hull, D. Husby, S.-I. Ichikawa, T. Ichikawa, Ž. Ivezić, S. Kent, R. S. J. Kim, E. Kinney, M. Klaene, A. N. Kleinman, S. Kleinman, G. R. Knapp, J. Korienek, R. G. Kron, P. Z. Kunszt, D. Q. Lamb, B. Lee, R. F. Leger, S. Limmongkol, C. Lindenmeyer, D. C. Long, C. Loomis, J. Loveday, R. Lucinio, R. H. Lupton, B. MacKinnon, E. J. Mannery, P. M. Mantsch, B. Margon, P. McGehee, T. A. McKay, A. Meiksin, A. Merelli, D. G. Monet, J. A. Munn, V. K. Narayanan, T. Nash, E. Neilsen, R. Neswold, H. J. Newberg, R. C. Nichol, T. Nicinski, M. Nonino, N. Okada, S. Okamura, J. P. Ostriker, R. Owen, A. G. Pauls, J. Peoples, R. L. Peterson, D. Petravick, J. R. Pier, A. Pope, R. Pordes, A. Prosapio, R. Rechenmacher, T. R. Quinn, G. T. Richards, M. W. Richmond, C. H. Rivetta, C. M. Rockosi, K. Ruthmansdorfer, D. Sandford, D. J. Schlegel, D. P. Schneider, M. Sekiguchi, G. Sergej, K. Shimasaku, W. A. Siegmund, S. Smee, J. A. Smith, S. Snedden, R. Stone, C. Stoughton, M. A. Strauss, C. Stubbs, M. SubbaRao, A. S. Szalay, I. Szapudi, G. P. Szokoly, A. R. Thakar, C. Tremonti, D. L. Tucker, A. Uomoto, D. Vanden Berk, M. S. Vogeley, P. Waddell, S.-i. Wang, M. Watanabe, D. H. Weinberg, B. Yanny, N. Yasuda, and SDSS Collaboration. The Sloan Digital Sky Survey: Technical Summary. , 120:1579–1587, September 2000. doi: 10.1086/301513.
- Y. B. Zel'dovich. The Fate of a Star and the Evolution of Gravitational Energy Upon Accretion. *Soviet Physics Doklady*, 9:195, September 1964.